Available online at www.sciencedirect.com
ScienceDirect
Comput. Methods Appl. Mech. Engrg. 279 (2014) 497–514
Computer methods in applied mechanics and engineering
www.elsevier.com/locate/cma

An unfitted Nitsche method for incompressible fluid–structure interaction using overlapping meshes

Erik Burman[a,*], Miguel A. Fernández[b,c]

[a] *Department of Mathematics, University College London, London, UK-WC1E 6BT, UK*
[b] *Inria, REO project-team, Rocquencourt, B.P. 105, F-78153 Le Chesnay Cedex, France*
[c] *UPMC Univ Paris VI, REO project-team, UMR 7958 LJLL, F-75005 Paris, France*

Received 21 December 2013; received in revised form 27 June 2014; accepted 5 July 2014
Available online 14 July 2014

Highlights

- Unfitted finite element method for a fluid–structure interaction.
- Proof of stability and accuracy.
- Different coupling scheme's for time advancement: fully coupled or loosely coupled.

Abstract

We consider the extension of the Nitsche method to the case of fluid–structure interaction problems on unfitted meshes. We give a stability analysis for the space semi-discretized problem and show how this estimate may be used to derive optimal error estimates for smooth solutions, irrespectively of the mesh/interface intersection. We also discuss different strategies for the time discretization, using either fully implicit or explicit coupling (*loosely coupled*) schemes. Some numerical examples illustrate the theoretical discussion.

Keywords: Fluid–structure interaction; Incompressible fluid; Unfitted meshes; Fictitious domain method; Nitsche method; Coupling schemes

1. Introduction

The use of Nitsche's method for the coupling of multiphysics problems in computational mechanics has received increasing attention recently (see, e.g., [1]). Thanks to its flexibility and the mathematical soundness it has been used to design methods for several problems. Examples include XFEM of elasticity, i.e., interface problems on unfitted meshes [2,3], and robust and accurate fictitious domain methods [4]. Nitsche's method was first applied to fluid–structure interaction problems in the framework of space–time Galerkin methods in [5] and used to design stable loosely coupled fluid–structure interaction methods in [6,7]. The objective of this note is to apply these techniques

* Corresponding author. Tel.: +44 7435605145.
E-mail address: e.burman@ucl.ac.uk (E. Burman).

http://dx.doi.org/10.1016/j.cma.2014.07.007

to design a computational method for fluid–structure interaction on unfitted meshes. The use of fictitious domain or immersed boundary methods for the numerical simulation of fluid–structure interaction problems was pioneered in the works [8–11] and has recently seen a surge of interest in papers such as [12–14].

Our contribution in the present paper is to show how Nitsche's method can be used for fluid–structure computations on unfitted meshes. We consider a low Reynolds regime (Stokes flow) and assume that the structure undergoes infinitesimal displacements (fixed interface). Though simplified, this setting retains some of the main numerical issues that appear in the time-stepping of complex non-linear incompressible fluid–structure interaction problems (see, e.g., [15]). We study both the case where the fluid and the solid equations are defined in domains of $\mathbb{R}^d$ and the case where the fluid is coupled to a thin-walled solid, with the solid equations written in the $(d-1)$-manifold defined by the fluid–solid interface. We present a rigorous proof that optimal convergence in energy norm is obtained for smooth solutions in the space semi-discretized case. Then we discuss different strategies for the time discretization, either fully implicit or the loosely coupled schemes introduced in [6,7].

We will study the case where the solid body is meshed and fitted to the interface. The main motivation for this is the fact that solids are generally described in Lagrangian coordinates and, hence, it is straightforward to move the mesh according to the deformation. This deformed solid mesh is then glued onto the fluid domain without respecting the mesh on the fluid side. This approach is similar to that proposed in [16] for the Poisson problem and more recently in [17] for Stokes' equations. The heterogeneous character of the present system however leads to some difficulties compared to these works. The Nitsche method uses explicit integration of normal stress on the interface to ensure consistency. Since the stress is continuous the stress may be taken from either the solid or the fluid system. Indeed in [16], robustness is ensured by taking all the stresses on the side where the mesh is conforming. This choice is convenient in the homogeneous case, but appears not to be so appealing in the case of fluid–structure interaction. The reason for this is that there is no dissipative mechanism in the solid elastodynamic system that can absorb the perturbation induced by the boundary stresses on the solid side.

If, on the other hand, the Nitsche mortaring is taken only from the fluid side as proposed in [5], the trace inequality necessary for the analysis is no longer robust and the penalty parameter may have to be chosen very large for unfortunate cuts of the mesh, or the resulting system matrix may turn out to be close to singular. In order to nevertheless design a robust and accurate method we suggest to use a ghost penalty term in the fluid (see [18,19] where this technique was proposed for fictitious domain methods for Stokes' problem) in order to extend the coercivity to all of the mesh domain. This is a weakly consistent stabilization term that extends the H^1-stability of the viscous dissipation, as well as the control of the fluid pressure, to the whole fluid mesh-domain, i.e., also to parts of cut elements that are outside the physical domain. We prove that this is sufficient for the method to be stable and optimally convergent.

It should be noted that, even though it appears non-physical, a similar analysis as the one presented below may be carried out if the stresses in the Nitsche coupling terms are taken on the solid side, provided that the solid equations are set in $\mathbb{R}^d$. This requires the use of Gronwall's inequality and leads to the appearance of an unspecified time scale in the Nitsche penalty parameter. Furthermore this approach is not feasible when thin-walled solids are considered and is very inconvenient for nonlinear elasticity. It will therefore not be discussed further herein.

An outline of the paper is as follows. In Section 2 we present a model problem for the fluid–structure interaction and the associated variational formulation. A Nitsche fictitious domain spatial discretization of the problem is proposed in Section 3. Stability and optimal convergence for smooth solutions is proven for this space semi-discretized system in Sections 3.1–3.3. Section 4 is devoted to time discretization, using either implicit or explicit coupling procedures. In Section 5 we present some numerical examples on a two-dimensional model problem. The performance of the fitted and the unfitted methods is compared. We investigate also the accuracy of the explicit coupling schemes proposed. Finally, Section 6 is dedicated to some concluding remarks.

2. A linear model problem

The physical domain consists of $\Omega \overset{\text{def}}{=} \Omega^{\text{f}} \cup \Omega^{\text{s}} \cup \Sigma \subset \mathbb{R}^d$, with $d = 2$ or 3, Ω^{f}, Ω^{s} the fluid and solid subdomains, respectively, and $\Sigma \overset{\text{def}}{=} \overline{\Omega^{\text{f}}} \cap \overline{\Omega^{\text{s}}}$ the fluid–solid interface. The exterior unit-vectors normal to $\partial\Omega^{\text{f}}$ and $\partial\Omega^{\text{s}}$ are denoted by $\boldsymbol{n}$ and $\boldsymbol{n}^{\text{s}}$. We consider partitions $\partial\Omega^{\text{f}} = \Gamma^{\text{f}} \cup \Sigma$ and $\partial\Omega^{\text{s}} = \Gamma^{\text{s}} \cup \Sigma$ of the fluid and solid boundaries. The fluid is described by the Stokes equations in the polyhedral domain Ω^{f}. For the structure we consider two cases, either the elastodynamics equations in $\Omega^{\text{s}} \subset \mathbb{R}^d$ or the elastodynamic equations for a thin-walled structure (string, membrane or shell) posed on the $(d-1)$-manifold Σ. In the latter case $\overline{\Omega^{\text{s}}} = \overline{\Sigma}$ and $\Gamma^{\text{s}} = \partial\Sigma$.

The considered coupled problem reads as follows: find the fluid velocity $\boldsymbol{u} : \Omega^{\mathrm{f}} \times \mathbb{R}^+ \to \mathbb{R}^d$ and the fluid pressure $p : \Omega^{\mathrm{f}} \times \mathbb{R}^+ \to \mathbb{R}$, satisfied in Ω^{f}, the solid displacement $\boldsymbol{d} : \Omega^{\mathrm{s}} \times \mathbb{R}^+ \to \mathbb{R}^d$ and the solid velocity $\dot{\boldsymbol{d}} : \Omega^{\mathrm{s}} \times \mathbb{R}^+ \to \mathbb{R}^d$ such that

$$\begin{cases} \rho^{\mathrm{f}} \partial_t \boldsymbol{u} - \mathbf{div}\, \boldsymbol{\sigma}(\boldsymbol{u}, p) = \mathbf{0} & \text{in } \Omega^{\mathrm{f}}, \\ \operatorname{div} \boldsymbol{u} = 0 & \text{in } \Omega^{\mathrm{f}}, \\ \boldsymbol{u} = \mathbf{0} & \text{on } \Gamma^{\mathrm{f},}, \end{cases} \tag{1}$$

$$\begin{cases} \dot{\boldsymbol{d}} = \partial_t \boldsymbol{d} & \text{in } \Omega^{\mathrm{s}}, \\ \rho^{\mathrm{s}} \partial_t \dot{\boldsymbol{d}} - \mathbf{div}\, \boldsymbol{\sigma}^{\mathrm{s}}(\boldsymbol{d}) = \mathbf{0} & \text{in } \Omega^{\mathrm{s}}, \\ \boldsymbol{d} = \mathbf{0} & \text{on } \Gamma^{\mathrm{s}}, \end{cases} \tag{2}$$

$$\begin{cases} \boldsymbol{u} = \dot{\boldsymbol{d}} & \text{on } \Sigma, \\ \boldsymbol{\sigma}(\boldsymbol{u}, p)\boldsymbol{n} = -\boldsymbol{\sigma}^{\mathrm{s}}(\boldsymbol{d})\boldsymbol{n}^{\mathrm{s}} & \text{on } \Sigma. \end{cases} \tag{3}$$

Here, ρ^{f} and ρ^{s} respectively denote the fluid and solid densities. The fluid Cauchy-stress tensor is given by

$$\boldsymbol{\sigma}(\boldsymbol{u}, p) \overset{\text{def}}{=} -p\boldsymbol{I} + 2\mu\boldsymbol{\epsilon}(\boldsymbol{u}), \quad \boldsymbol{\epsilon}(\boldsymbol{u}) \overset{\text{def}}{=} \frac{1}{2}\left(\boldsymbol{\nabla u} + \boldsymbol{\nabla u}^{\mathrm{T}}\right),$$

where μ stands for the fluid dynamic viscosity and $\boldsymbol{I}$ the identity matrix in $\mathbb{R}^d$. The solid stress tensor is given by

$$\boldsymbol{\sigma}^{\mathrm{s}}(\boldsymbol{d}) \overset{\text{def}}{=} 2L_1\boldsymbol{\epsilon}(\boldsymbol{d}) + L_2(\operatorname{div}\boldsymbol{d})\boldsymbol{I},$$

where $L_1, L_2 > 0$ stand for the Lamé constants of the structure. This system of equations is complemented with the initial conditions $\boldsymbol{u}(0) = \boldsymbol{u}^0$, $\boldsymbol{d}(0) = \boldsymbol{d}^0$, $\dot{\boldsymbol{d}}(0) = \dot{\boldsymbol{d}}^0$.

In the case of the coupling with a thin-walled structure, the relations (2)–(3) are replaced by

$$\begin{cases} \boldsymbol{u} = \dot{\boldsymbol{d}} & \text{in } \Sigma, \\ \rho^{\mathrm{s}}\epsilon\,\partial_t\dot{\boldsymbol{d}} + \boldsymbol{L}^{\mathrm{e}}\boldsymbol{d} = -\boldsymbol{\sigma}(\boldsymbol{u}, p)\boldsymbol{n} & \text{in } \Sigma, \\ \dot{\boldsymbol{d}} = \partial_t\boldsymbol{d} & \text{in } \Sigma, \\ \boldsymbol{d} = \mathbf{0} & \text{on } \Gamma^{\mathrm{s}}, \end{cases} \tag{4}$$

where $\boldsymbol{L}^{\mathrm{e}}$ denotes an elasticity operator defined on the $(d-1)$-manifold Σ and ϵ denotes the thickness of the structure. Note that $(4)_2$ simultaneously enforces the kinetic continuity and the momentum equilibrium in the solid. Well-posedness results for this type of linear fluid–structure interaction problems can be found in [20,21].

In what follows, we will consider the usual Sobolev spaces $H^m(\omega)$ $(m \geq 0)$, with norm $\|\cdot\|_{m,\omega}$ and semi-norm $|\cdot|_{m,\omega}$. For a given part $\Gamma \subset \partial\omega$ of $\partial\omega$, the closed subspace $H^1_{\Gamma}(\omega)$, consisting of functions in $H^1(\omega)$ with zero trace on Γ, will be used. The scalar product in $L^2(\omega)$ is denoted by $(\cdot,\cdot)_\omega$ and its norm by $\|\cdot\|_{0,\omega}$.

For the weak formulation of the solid system (2) we introduce the space of admissible displacements $\boldsymbol{W} \overset{\text{def}}{=} [H^1_{\Gamma^{\mathrm{s}}}(\Omega^{\mathrm{s}})]^d$ and the elastic bi-linear form $a^{\mathrm{e}} : \boldsymbol{W} \times \boldsymbol{W} \to \mathbb{R}$ defined by

$$a^{\mathrm{e}}(\boldsymbol{d}, \boldsymbol{w}) \overset{\text{def}}{=} 2L_1\big(\boldsymbol{\epsilon}(\boldsymbol{d}), \boldsymbol{\epsilon}(\boldsymbol{w})\big)_{\Omega^{\mathrm{s}}} + L_2\big(\operatorname{div}\boldsymbol{d}, \operatorname{div}\boldsymbol{w}\big)_{\Omega^{\mathrm{s}}},$$

for all $\boldsymbol{d}, \boldsymbol{w} \in \boldsymbol{W}$. In the case of a thin-walled structure the elastic bilinear form is simply defined as the weak form of the differential surface operator $\boldsymbol{L}^{\mathrm{e}}$, that we assume to be symmetric, coercive and continuous on $\boldsymbol{W}$. An example will be given in Section 5. We define the elastic energy norm by $\|\boldsymbol{w}\|_{\mathrm{e}} \overset{\text{def}}{=} a^{\mathrm{e}}(\boldsymbol{w}, \boldsymbol{w})^{\frac{1}{2}}$. We also introduce the fluid velocity and pressure functional spaces $\boldsymbol{V} \overset{\text{def}}{=} [H^1_{\Gamma^{\mathrm{f}}}(\Omega^{\mathrm{f}})]^d$, $Q \overset{\text{def}}{=} L^2(\Omega^{\mathrm{f}})$. Finally, the standard bi-linear forms for the Stokes problem, $a : \boldsymbol{V} \times \boldsymbol{V} \to \mathbb{R}$ and $b : Q \times \boldsymbol{V} \to \mathbb{R}$, given by

$$a(\boldsymbol{u}, \boldsymbol{v}) \overset{\text{def}}{=} 2\mu\big(\boldsymbol{\epsilon}(\boldsymbol{u}), \boldsymbol{\epsilon}(\boldsymbol{v})\big)_{\Omega^{\mathrm{f}}}, \qquad b(q, \boldsymbol{v}) \overset{\text{def}}{=} -(q, \operatorname{div}\boldsymbol{v})_{\Omega^{\mathrm{f}}},$$

will be used.

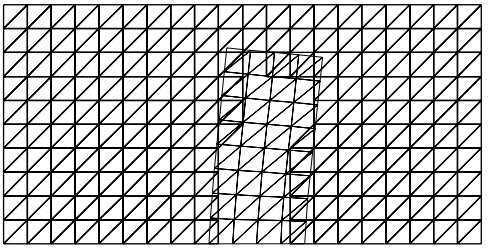

Fig. 1. Example of overlapping fluid–solid meshes.

3. Space semi-discretization: Nitsche fictitious domain formulation

Let $\{\mathcal{T}_h^{\mathrm{s}}\}_{0<h\leq 1}$ denote a family of triangulations of Ω^{s}. The meshes $\mathcal{T}_h^{\mathrm{s}}$ are fitted to Ω^{s}. Then consider a family of meshes $\{\mathcal{T}_h^{\mathrm{f}}\}_{0<h\leq 1}$, where each $\mathcal{T}_h^{\mathrm{f}}$ covers the fluid region Ω^{f}, $\mathcal{T}_h^{\mathrm{f}} \subset \Omega^{\mathrm{f}}$ and is fitted to the Dirichlet boundaries Γ^{f}, but in general not to Σ. Instead we assume that for every simplex $K \in \mathcal{T}_h^{\mathrm{f}}$ there holds $K \cap \Omega^{\mathrm{f}} \neq \emptyset$ (see Fig. 1). We have, in particular,

$$\overline{\Omega^{\mathrm{s}}} = \bigcup_{K\in\mathcal{T}_h^{\mathrm{s}}}, \qquad \overline{\Omega^{\mathrm{f}}} \subsetneq \bigcup_{K\in\mathcal{T}_h^{\mathrm{f}}}.$$

We will denote by $\Omega^{\mathrm{f}}_{\mathcal{T}_h}$ the set of $\mathbb{R}^d$ coinciding with $\mathcal{T}_h^{\mathrm{f}}$, that is, $\overline{\Omega^{\mathrm{f}}_{\mathcal{T}_h}} \stackrel{\mathrm{def}}{=} \cup_{K\in\mathcal{T}_h^{\mathrm{f}}}$. For each triangulation $\mathcal{T}_h$, the subscript $h \in (0, 1]$ refers to the level of refinement of the triangulation, which is defined by $h \stackrel{\mathrm{def}}{=} \max_{K\in\mathcal{T}_h} h_K$, with h_K the diameter of K. In order to simplify the presentation, we assume that the families of triangulations are quasi-uniform.

We will use the following discrete semi-norms on function values on the interface Σ,

$$\|u\|_{\pm\frac{1}{2},h,\Sigma} \stackrel{\mathrm{def}}{=} \left(\sum_{\{K\in\mathcal{T}_h^{\mathrm{f}}:K\cap\Sigma\neq\emptyset\}} \int_{K\cap\Sigma} h_K^{\mp 1}|u|^2\right)^{\frac{1}{2}}.$$

We also note that the following trace inequality holds for all functions in $H^1(K)$. There exists $C_{\mathrm{T}} > 0$ such that for the intersection of the polygonal/polyhedral surface Σ with an element K there holds

$$\|u\|_{0,K\cap\Sigma} \leq C_{\mathrm{T}}\left(h^{-\frac{1}{2}}\|u\|_{0,K} + h^{\frac{1}{2}}\|\nabla u\|_{0,K}\right). \tag{5}$$

For shape regular elements, the proof of this result is equivalent to that of the standard trace inequality.

In what follows, we consider the standard spaces of continuous piecewise affine functions:

$$\begin{aligned} X_h^{\mathrm{f}} &\stackrel{\mathrm{def}}{=} \left\{v_h \in C^0(\overline{\Omega^{\mathrm{f}}_{\mathcal{T}_h}}) \,/\, v_{h|K} \in \mathbb{P}_1(K)\ \forall K \in \mathcal{T}_h^{\mathrm{f}}\right\}, \\ X_h^{\mathrm{s}} &\stackrel{\mathrm{def}}{=} \left\{v_h \in C^0(\overline{\Omega^{\mathrm{s}}}) \,/\, v_{h|K} \in \mathbb{P}_1(K)\ \forall K \in \mathcal{T}_h^{\mathrm{s}}\right\}. \end{aligned} \tag{6}$$

For the approximation of the fluid velocity we will consider the space

$$\boldsymbol{V}_h \stackrel{\mathrm{def}}{=} \left\{\boldsymbol{v}_h \in [X_h^{\mathrm{f}}]^d \,/\, \boldsymbol{v}_h|_{\Gamma^{\mathrm{f}}} = 0\right\}$$

and for the pressure we will use $Q_h \stackrel{\mathrm{def}}{=} X_h^{\mathrm{f}}$. Observe that for $q_h \in Q_h$ we have $q_h|_{\Omega^{\mathrm{f}}} \in Q$. For the solid we set $\boldsymbol{W}_h \stackrel{\mathrm{def}}{=} [X_h^{\mathrm{s}}]^d \cap \boldsymbol{W}$.

Since our choice of velocity and pressure spaces does not satisfy the inf–sup condition, we will consider a pressure stabilization in the form of an operator $s_h : Q_h \times Q_h \mapsto \mathbb{R}$ in the mass equation below. We assume that the pressure stabilization operator, $s_p : Q_h \times Q_h \to \mathbb{R}$, satisfies

$$c_1\mu^{-1}h^2|p_h|^2_{1,\Omega^{\mathrm{f}}_{\mathcal{T}_h}} \leq s_h(p_h, p_h) \leq c_2\mu^{-1}h^2|p_h|^2_{1,\Omega^{\mathrm{f}}_{\mathcal{T}_h}}, \tag{7}$$

with $c_1, c_2 > 0$. For instance, the classical Brezzi–Pitkäranta pressure stabilization [22] may be used on the following form

$$s_h(p_h, q_h) \overset{\text{def}}{=} \gamma_{\text{p}} \int_{\Omega^{\text{f}}_{\mathcal{T}}} \frac{h^2}{\mu} \nabla p_h \cdot \nabla q_h, \quad \gamma_{\text{p}} > 0. \tag{8}$$

Observe that the pressure stabilization is defined over the computational fluid domain $\Omega^{\text{f}}_{\mathcal{T}}$. This feature is crucial to ensure stability for the coupling over the unfitted boundary. To counter instabilities due to the cut meshes we introduce a penalty term on the fluid velocities as well, $g_h : \boldsymbol{V}_h \times \boldsymbol{V}_h \to \mathbb{R}$, we assume that this operator is designed so that the following stability holds:

$$\tilde{c}_{\text{s}} \left(\mu \|\boldsymbol{\epsilon}(\boldsymbol{v}_h)\|^2_{0,\Omega^{\text{f}}_{\mathcal{T}_h}} + g_h(\boldsymbol{v}_h, \boldsymbol{v}_h) \right) \leq \mu \|\boldsymbol{\epsilon}(\boldsymbol{v}_h)\|^2_{0,\Omega^{\text{f}}} + g_h(\boldsymbol{v}_h, \boldsymbol{v}_h) \tag{9}$$

for all $\boldsymbol{v}_h \in \boldsymbol{V}_h$ and with $\tilde{c}_{\text{s}} > 0$ (see [18] for examples of suitable operators and a proof). The role of g_h is to extend the coercivity from the fluid domain Ω^{f} to the computational domain $\Omega^{\text{f}}_{\mathcal{T}_h}$. This feature allows us to prove robust error estimates independent of the mesh interface intersection. Note that the velocity stabilization only is needed in the interface zone and can in principle even be localized to elements K for which $\Omega^{\text{f}} \cap K$ is small.

We denote the total fluid stabilization by

$$S_h\big((\boldsymbol{u}_h, p_h), (\boldsymbol{v}_h, q_h)\big) \overset{\text{def}}{=} s_h(p_h, q_h) + g_h(\boldsymbol{u}_h, \boldsymbol{v}_h), \tag{10}$$

with associated semi-norm $|(u_h, p_h)|_S \overset{\text{def}}{=} S_h\big((\boldsymbol{u}_h, p_h), (\boldsymbol{u}_h, p_h)\big)^{\frac{1}{2}}$. The proposed space semi-discrete approximation of the systems given by (1)–(3) or (1) and (1)–(4) reads as follows: for $t > 0$, find

$$\big(\boldsymbol{u}_h(t), p_h(t), \dot{\boldsymbol{d}}_h(t), \boldsymbol{d}_h(t)\big) \in \boldsymbol{V}_h \times Q_h \times \boldsymbol{W}_h \times \boldsymbol{W}_h,$$

such that $\dot{\boldsymbol{d}}_h(t) = \partial_t \boldsymbol{d}_h(t)$ and

$$\begin{cases} \rho^{\text{f}}\big(\partial_t \boldsymbol{u}_h, \boldsymbol{v}_h\big)_{\Omega^{\text{f}}} + A\big((\boldsymbol{u}_h, p_h), (\boldsymbol{v}_h, q_h)\big) + \rho^{\text{s}}\big(\partial_t \dot{\boldsymbol{d}}_h, \boldsymbol{w}_h\big)_{\Omega^{\text{s}}} + a^{\text{e}}(\boldsymbol{d}_h, \boldsymbol{w}_h) \\ \quad - \big(\boldsymbol{\sigma}(\boldsymbol{u}_h, p_h)\boldsymbol{n}, (\boldsymbol{v}_h - \boldsymbol{w}_h)\big)_{\Sigma} - \big((\boldsymbol{u}_h - \dot{\boldsymbol{d}}_h), \boldsymbol{\sigma}(\boldsymbol{v}_h, -q_h)\boldsymbol{n}\big)_{\Sigma} \\ \quad + \dfrac{\gamma\mu}{h}\big((\boldsymbol{u}_h - \dot{\boldsymbol{d}}_h), (\boldsymbol{v}_h - \boldsymbol{w}_h)\big)_{\Sigma} + S_h\big((\boldsymbol{u}_h, p_h), (\boldsymbol{v}_h, q_h)\big) = 0 \end{cases} \tag{11}$$

for all $(\boldsymbol{v}_h, q_h, \boldsymbol{w}_h) \in \boldsymbol{V}_h \times Q_h \times \boldsymbol{W}_h$. Here, we have used the notation

$$A\big((\boldsymbol{u}_h, p_h), (\boldsymbol{v}_h, q_h)\big) \overset{\text{def}}{=} a(\boldsymbol{u}_h, \boldsymbol{v}_h) + b(p_h, \boldsymbol{v}_h) - b(q_h, \boldsymbol{u}_h)$$

and $\gamma > 0$ is the Nitsche penalty parameter.

Remark 3.1. Note that the integrals in the bilinear forms corresponding to the fluid model are evaluated over the physical domain Ω^{f}. This means that, in practice, numerical quadrature has to be performed over the parts of the triangles that intersect the physical fluid domain. This is a non-standard implementational problem that has been discussed in [23].

Remark 3.2. Note that the fluid mass matrix may be poorly conditioned if some nodes have macroelements with very small intersection with the physical domain. The space discretization operator of the fluid system however will have a condition number that is uniform in the mesh-interface intersection (see [17] for a proof) and therefore ill-conditioning of the mass matrix is unlikely to have any impact on the full system, except for very small time-step. This problem can be eliminated using diagonal scaling or alternatively the mass matrix can be stabilized as well using an operator similar to $g_h(\cdot, \cdot)$, to extend the L^2-stability to the computational domain $\Omega^{\text{f}}_{\mathcal{T}_h}$. This only requires a modification of the parameter of $g_h(\cdot, \cdot)$.

3.1. Stability properties of the discrete scheme

The next lemma states a result giving the coercivity in $\Omega^{\text{f}}_{\mathcal{T}_h}$ of the discretization of Stokes' system.

Lemma 3.1. *For $\gamma > 0$ sufficiently large, there exists $c_s > 0$ such that*

$$c_s \left(\mu \|\nabla \boldsymbol{v}_h\|^2_{0,\Omega^f_{\mathcal{T}}} + \gamma\mu \|\boldsymbol{v}_h - \boldsymbol{w}_h\|^2_{\frac{1}{2},h,\Sigma} + |(\boldsymbol{v}_h, q_h)|^2_S \right) \leq A\Big((\boldsymbol{v}_h, q_h), (\boldsymbol{v}_h, q_h)\Big) - \big(\boldsymbol{\sigma}(\boldsymbol{v}_h, q_h)\boldsymbol{n}, (\boldsymbol{v}_h - \boldsymbol{w}_h)\big)_\Sigma$$
$$- \big(\boldsymbol{\sigma}(\boldsymbol{v}_h, -q_h)\boldsymbol{n}, \boldsymbol{v}_h - \boldsymbol{w}_h\big)_\Sigma + \frac{\gamma\mu}{h}\big(\boldsymbol{v}_h - \boldsymbol{w}_h, \boldsymbol{v}_h - \boldsymbol{w}_h\big)_\Sigma + |(\boldsymbol{v}_h, q_h)|^2_S$$

for all $(\boldsymbol{v}_h, q_h) \in \boldsymbol{V}_h \times Q_h$ and $\boldsymbol{w}_h \in \boldsymbol{W}_h$.

Proof. Note that

$$A\Big((\boldsymbol{v}_h, p_h), (\boldsymbol{v}_h, p_h)\Big) - \big(\boldsymbol{\sigma}(\boldsymbol{v}_h, p_h)\boldsymbol{n}, (\boldsymbol{v}_h - \boldsymbol{w}_h)\big)_\Sigma$$
$$- \big(\boldsymbol{\sigma}(\boldsymbol{v}_h, -p_h)\boldsymbol{n}, \boldsymbol{v}_h - \boldsymbol{w}_h\big)_\Sigma + \frac{\gamma\mu}{h}\big(\boldsymbol{v}_h - \boldsymbol{w}_h, \boldsymbol{v}_h - \boldsymbol{w}_h\big)_\Sigma + |(\boldsymbol{v}_h, p_h)|^2_S$$
$$= 2\mu \|\boldsymbol{\epsilon}(\boldsymbol{v}_h)\|^2_{0,\Omega^f} - 2\big(\boldsymbol{\sigma}(\boldsymbol{v}_h, 0)\boldsymbol{n}, (\boldsymbol{v}_h - \boldsymbol{w}_h)\big)_\Sigma + \gamma\mu \|\boldsymbol{v}_h - \boldsymbol{w}_h\|^2_{\frac{1}{2},h,\Sigma} + |(\boldsymbol{v}_h, p_h)|^2_S.$$

We now observe that, by combining (5) with a discrete inverse inequality, it follows that

$$\big(\boldsymbol{\sigma}(\boldsymbol{v}_h, 0)\boldsymbol{n}, \boldsymbol{v}_h - \boldsymbol{w}_h\big)_\Sigma \leq 2\frac{C_{TI}}{\gamma^{\frac{1}{2}}} \mu^{\frac{1}{2}} \|\boldsymbol{\epsilon}(\boldsymbol{v}_h)\|_{0,\Omega^f_{\mathcal{T}_h}} \gamma^{\frac{1}{2}} \mu^{\frac{1}{2}} \|\boldsymbol{v}_h - \boldsymbol{w}_h\|_{\frac{1}{2},h,\Sigma},$$

with $C_{TI} > 0$. Finally, we conclude by using an arithmetic–geometric inequality with suitable weights, the stability estimate (9), Korn's inequality and taking γ sufficiently large. □

If we take $\boldsymbol{v}_h = \boldsymbol{u}_h$, $q_h = p_h$ and $\boldsymbol{w}_h = \dot{\boldsymbol{d}}_h$ in (11) and apply the result of Lemma 3.1 we get the following energy inequality:

$$\frac{\mathrm{d}}{\mathrm{d}t}\left(\frac{\rho^f}{2} \|\boldsymbol{u}_h\|^2_{0,\Omega^f} + \frac{\rho^s}{2} \|\dot{\boldsymbol{d}}_h\|^2_{0,\Omega^s} + a^e(\boldsymbol{d}_h, \boldsymbol{d}_h) \right)$$
$$+ c_s \left(\mu \|\nabla \boldsymbol{u}_h\|^2_{0,\Omega^f_{\mathcal{T}_h}} + \gamma\mu \|\boldsymbol{u}_h - \dot{\boldsymbol{d}}_h\|^2_{\frac{1}{2},h,\Sigma} + |(\boldsymbol{u}_h, p_h)|^2_S \right) \leq 0, \tag{12}$$

which guarantees the energy stability of the unfitted space semi-discrete approximation (11).

3.2. Consistency of the formulation

If we multiply (1) by $\boldsymbol{v}_h, q_h \in \boldsymbol{V}_h \times Q_h$ and (2) by $\boldsymbol{w}_h \in \boldsymbol{W}_h$, integrate by parts in both systems and use $(3)_2$, we obtain the equality

$$\rho^f\big(\partial_t \boldsymbol{u}, \boldsymbol{v}_h\big)_{\Omega^f} + A\Big((\boldsymbol{u}, p), (\boldsymbol{v}_h, q_h)\Big) + \rho^s\big(\partial_t \dot{\boldsymbol{d}}, \boldsymbol{w}_h\big)_{\Omega^s} + a^e(\boldsymbol{d}, \boldsymbol{w}_h) - \big(\boldsymbol{\sigma}(\boldsymbol{u}, p)\boldsymbol{n}, (\boldsymbol{v}_h - \boldsymbol{w}_h)\big)_\Sigma = 0.$$

The same result is obtained for (1), (4), this time with the coupling conditions given in $(4)_2$. Hence, owing to $(3)_1$ or $(4)_1$, we may write

$$\rho^f\big(\partial_t \boldsymbol{u}, \boldsymbol{v}_h\big)_{\Omega^f} + A\Big((\boldsymbol{u}, p), (\boldsymbol{v}_h, q_h)\Big) + \rho^s\big(\partial_t \dot{\boldsymbol{d}}, \boldsymbol{w}_h\big)_{\Omega^s} + a^e(\boldsymbol{d}, \boldsymbol{w}_h)$$
$$- \big(\boldsymbol{\sigma}(\boldsymbol{u}, p)\boldsymbol{n}, (\boldsymbol{v}_h - \boldsymbol{w}_h)\big)_\Sigma - \big((\boldsymbol{u} - \dot{\boldsymbol{d}}), \boldsymbol{\sigma}(\boldsymbol{v}_h, -q_h)\boldsymbol{n}\big)_\Sigma + \frac{\gamma\mu}{h}\big((\boldsymbol{u} - \dot{\boldsymbol{d}}), (\boldsymbol{v}_h - \boldsymbol{w}_h)\big)_\Sigma = 0 \tag{13}$$

for all $\boldsymbol{v}_h, q_h, \boldsymbol{w}_h \in \boldsymbol{V}_h \times Q_h \times \boldsymbol{W}_h$. Taking the difference between (13) and (11) we obtain the following result.

Lemma 3.2 (*Galerkin Orthogonality*)**.** *Let $(\boldsymbol{u}, p, \dot{\boldsymbol{d}}, \boldsymbol{d})$ be the solution of (1), (2), (3) or (1), (4) and $(\boldsymbol{u}_h, p_h, \dot{\boldsymbol{d}}_h, \boldsymbol{d}_h)$ be given by (11). The following approximate Galerkin orthogonality holds:*

$$\rho^f\big(\partial_t(\boldsymbol{u} - \boldsymbol{u}_h), \boldsymbol{v}_h\big)_{\Omega^f} + A\Big((\boldsymbol{u} - \boldsymbol{u}_h, p - p_h), (\boldsymbol{v}_h, q_h)\Big) + \rho^s\big(\partial_t(\dot{\boldsymbol{d}} - \dot{\boldsymbol{d}}_h), \boldsymbol{w}_h\big)_{\Omega^s}$$
$$+ a^e(\boldsymbol{d} - \boldsymbol{d}_h, \boldsymbol{w}_h) - \big(\boldsymbol{\sigma}(\boldsymbol{u} - \boldsymbol{u}_h, p - p_h)\boldsymbol{n}, (\boldsymbol{v}_h - \boldsymbol{w}_h)\big)_\Sigma$$
$$- \big((\boldsymbol{u} - \boldsymbol{u}_h) - (\dot{\boldsymbol{d}} - \dot{\boldsymbol{d}}_h), \boldsymbol{\sigma}(\boldsymbol{v}_h, -q_h)\boldsymbol{n}\big)_\Sigma + \frac{\gamma\mu}{h}\big((\boldsymbol{u} - \boldsymbol{u}_h) - (\dot{\boldsymbol{d}} - \dot{\boldsymbol{d}}_h), (\boldsymbol{v}_h - \boldsymbol{w}_h)\big)_\Sigma$$
$$= S_h\big((\boldsymbol{u}_h, p_h), (\boldsymbol{v}_h, q_h)\big) \tag{14}$$

for all $\boldsymbol{v}_h, q_h, \boldsymbol{w}_h \in \boldsymbol{V}_h \times Q_h \times \boldsymbol{W}_h$ and $t > 0$.

3.3. Error analysis

In the succeeding text, the symbol $\lesssim$ indicates inequalities up to a multiplicative constant (independent of the discretization parameter h and the mesh/interface intersection). Furthermore, we assume that the elements in the solid mesh with faces in the solid trace mesh on Σ may be grouped in disjoint macropatches P_i, with $\text{meas}(P_i) = \mathcal{O}(h^d)$ in the case of a thick-walled solid and $\text{meas}(P_i) = \mathcal{O}(h^{d-1})$ for a thin-walled solid. The restriction of the patch P_i to Σ will be denoted by $F_i \overset{\text{def}}{=} P_i \cap \Sigma$. In the case of thin-walled solids we have $P_i \equiv F_i$. Each $(d-1)$-dimensional macropatch F_i is assumed to contain at least one interior node and the union of the F_i is assumed to cover Σ, viz., $\cup_i F_i = \Sigma$.

We introduce the discrete solid errors

$$\boldsymbol{\xi}_h \overset{\text{def}}{=} \boldsymbol{d}_h - \pi_h^{\text{e}}\boldsymbol{d}, \qquad \dot{\boldsymbol{\xi}}_h \overset{\text{def}}{=} \dot{\boldsymbol{d}}_h - \mathcal{I}_h\dot{\boldsymbol{d}} \quad \text{in } \Omega^{\text{s}},$$

where π_h^{e} stands for the elastic Ritz-projection of the solid, viz., $a^{\text{e}}(\boldsymbol{d} - \pi_h^{\text{e}}\boldsymbol{d}, \boldsymbol{w}_h) = 0$ for all $\boldsymbol{w}_h \in \boldsymbol{W}_h$. We assume that the solid is convex so that $\|\pi_h^{\text{e}}\boldsymbol{d} - \boldsymbol{d}\|_{0,\Omega^{\text{s}}} \lesssim h^2|\boldsymbol{d}|^2_{2,\Omega^{\text{s}}}$. The interpolation operator $\mathcal{I}_h$ is defined by

$$\mathcal{I}_h\dot{\boldsymbol{d}} \overset{\text{def}}{=} \pi_h^{\text{e}}\dot{\boldsymbol{d}} + \sum_i \alpha_i \boldsymbol{\varphi}_i,$$

with $\alpha_i \in \mathbb{R}$. The $\boldsymbol{\varphi}_i$ are functions with support in the patches P_i, such that $0 \le \boldsymbol{\varphi}_i \le 1$, with $\|\boldsymbol{\varphi}_i\|_{0,P_i} \lesssim h^{\frac{d}{2}}$ for the thick-walled solid case and $\|\boldsymbol{\varphi}_i\|_{0,P_i} \lesssim h^{\frac{d-1}{2}}$ for the thin-walled solid case. The function $\boldsymbol{\varphi}_i$ takes the value 1, component-wise, in the interior nodes of the associated interface patch F_i. The associated α_i are chosen so that

$$\int_{F_i} (\dot{\boldsymbol{d}} - \mathcal{I}_h\dot{\boldsymbol{d}}) \cdot \boldsymbol{n} = 0. \tag{15}$$

For details on the construction of $\boldsymbol{\varphi}_i$ we refer to [24].

We now assume that there exist two linear continuous lifting operators $E_2 : H^2(\Omega^{\text{f}}) \to H^2(\mathbb{R}^d)$ and $E_1 : H^1(\Omega^{\text{f}}) \to H^1(\mathbb{R}^d)$, satisfying the bounds $\|E_1 v\|_{H^1(\mathbb{R}^d)} \lesssim \|v\|_{H^1(\Omega^{\text{f}})}$ for all $v \in H^1(\Omega^{\text{f}})$ and $\|E_2 v\|_{H^2(\mathbb{R}^d)} \lesssim \|v\|_{H^2(\Omega^{\text{f}})}$ for all $v \in H^2(\Omega^{\text{f}})$. Using these lifting operators (component wise) we introduce the discrete errors for the fluid

$$\boldsymbol{\theta}_h \overset{\text{def}}{=} \boldsymbol{u}_h - i_{\text{sz}}E_2\boldsymbol{u}, \qquad y_h \overset{\text{def}}{=} p_h - i_{\text{sz}}E_1 p \quad \text{in } \Omega^{\text{f}}_{\mathcal{T}_h},$$

where i_{sz} is defined by the Scott–Zhang interpolant (see, e.g., [25]). We assume that the stabilization operator defined in (10) satisfies the following weak consistency property

$$\left|\left(i_{\text{sz}}E_2\boldsymbol{u}, i_{\text{sz}}E_1 p\right)\right|_S \lesssim h\left(\mu^{\frac{1}{2}}|\boldsymbol{u}|_{2,\Omega^{\text{f}}} + \mu^{-\frac{1}{2}}|p|_{1,\Omega^{\text{f}}}\right). \tag{16}$$

For a proof of this property for the velocity part we refer to [4]. The pressure part is an immediate consequence of (7), the H^1-stability of the Scott–Zhang interpolant and the stability of the extension operator E_1,

$$s_h\left(i_{\text{sz}}E_1 p, i_{\text{sz}}E_1 p\right)^{\frac{1}{2}} \lesssim \mu^{-\frac{1}{2}}h|i_{\text{sz}}E_1 p|_{1,\Omega^{\text{f}}_{\mathcal{T}_h}} \lesssim \mu^{-\frac{1}{2}}h|E_1 p|_{1,\Omega^{\text{f}}_{\mathcal{T}_h}} \lesssim \mu^{-\frac{1}{2}}h|p|_{1,\Omega^{\text{f}}}.$$

The remaining necessary approximation estimates for these interpolants are collected in the following lemma.

Lemma 3.3. *Assume that $\boldsymbol{u} \in [H^2(\Omega^{\text{f}})]^d$, $p \in H^1(\Omega^{\text{f}})$ and $\boldsymbol{d}, \dot{\boldsymbol{d}} \in [H^2(\Omega^{\text{s}})]^d$. The following approximation estimates hold:*

$$\|\boldsymbol{u} - i_{\text{sz}}E_2\boldsymbol{u}\|_{0,\Omega^{\text{f}}} + h\|\nabla(\boldsymbol{u} - i_{\text{sz}}E_2\boldsymbol{u})\|_{0,\Omega^{\text{f}}} \lesssim h^2|\boldsymbol{u}|_{2,\Omega^{\text{f}}},$$

$$\|p - i_{\text{sz}}E_1 p\|_{0,\Omega^{\text{f}}} + h\|\nabla(p - i_{\text{sz}}E_1 p)\|_{0,\Omega^{\text{f}}} \lesssim h|p|_{1,\Omega^{\text{f}}},$$

$$\|\boldsymbol{d} - \pi_h^{\text{e}}\boldsymbol{d}\|_{0,\Omega^{\text{s}}} + h\|\nabla(\boldsymbol{d} - \pi_h^{\text{e}}\boldsymbol{d})\|_{0,\Omega^{\text{s}}} \lesssim h^2|\boldsymbol{d}|_{2,\Omega^{\text{s}}},$$

$$\|\dot{\boldsymbol{d}} - \mathcal{I}_h\dot{\boldsymbol{d}}\|_{0,\Omega^{\text{s}}} + h\|\nabla(\dot{\boldsymbol{d}} - \mathcal{I}_h\dot{\boldsymbol{d}})\|_{0,\Omega^{\text{s}}} \lesssim h^2|\dot{\boldsymbol{d}}|_{2,\Omega^{\text{s}}},$$

$$\|\boldsymbol{\sigma}(\boldsymbol{u} - i_{\text{sz}}E_2\boldsymbol{u}, p - i_{\text{sz}}E_1 p)\boldsymbol{n}\|_{-\frac{1}{2},h,\Sigma} \lesssim h\left(\|\boldsymbol{u}\|_{2,\Omega^{\text{f}}} + \|p\|_{1,\Omega^{\text{f}}}\right),$$

$$\|(\boldsymbol{u} - i_{\text{sz}}E_2\boldsymbol{u}) - (\dot{\boldsymbol{d}} - \mathcal{I}_h\dot{\boldsymbol{d}})\|_{\frac{1}{2},h,\Sigma} \lesssim h\left(\|\boldsymbol{u}\|_{2,\Omega^{\text{f}}} + \|\dot{\boldsymbol{d}}\|_{2,\Omega^{\text{s}}}\right).$$

Proof. We only discuss the proof of the three last estimates, since the other estimates follow using standard approximation theory and the stability of the extension operator. By the construction of $\mathcal{I}_h$ we have,

$$\alpha_i = \frac{\int_{F_i} (\dot{\boldsymbol{d}} - \pi_h^{\mathrm{e}} \dot{\boldsymbol{d}}) \cdot \boldsymbol{n}}{\int_{F_i} \boldsymbol{\varphi}_i \cdot \boldsymbol{n}}.$$

Since $h^{(d-1)} \lesssim |\int_{F_i} \boldsymbol{\varphi}_i \cdot \boldsymbol{n}|$ and $\mathrm{meas}(F_i) = \mathcal{O}(h^{d-1})$, we have

$$\sum_i |\alpha_i|^2 \lesssim \sum_i \left(\frac{\left| \int_{F_i} (\dot{\boldsymbol{d}} - \pi_h^{\mathrm{e}} \dot{\boldsymbol{d}}) \cdot \boldsymbol{n} \right|}{h^{(d-1)}} \right)^2 \lesssim h^{1-d} \sum_i \|\dot{\boldsymbol{d}} - \pi_h^{\mathrm{e}} \dot{\boldsymbol{d}}\|_{0,F_i}^2. \tag{17}$$

Therefore, for the thick-walled solid, there holds

$$\sum_i |\alpha_i|^2 \lesssim h^{4-d} |\dot{\boldsymbol{d}}|_{2,\Omega^{\mathrm{s}}}^2, \tag{18}$$

where the last inequality follows from (5) and the approximation properties of π_h^{e}. For the thin-walled solid case, thanks to the approximation properties of π_h^{e}, we get

$$\sum_i |\alpha_i|^2 \lesssim h^{5-d} |\dot{\boldsymbol{d}}|_{2,\Omega^{\mathrm{s}}}^2. \tag{19}$$

Hence, for the thick-walled solid, it follows that

$$\|\dot{\boldsymbol{d}} - \mathcal{I}_h \dot{\boldsymbol{d}}\|_{0,\Omega^{\mathrm{s}}} \leq \|\dot{\boldsymbol{d}} - \pi_h^{\mathrm{e}} \dot{\boldsymbol{d}}\|_{0,\Omega^{\mathrm{s}}} + \left(\sum_i \|\alpha_i \boldsymbol{\varphi}_i\|_{0,P_i}^2 \right)^{\frac{1}{2}} \lesssim h^2 |\dot{\boldsymbol{d}}|_{2,\Omega^{\mathrm{s}}} + \left(h^d \sum_i |\alpha_i|^2 \right)^{\frac{1}{2}}$$

and we conclude by applying (18). Whereas, for the thin-walled solid, we have

$$\|\dot{\boldsymbol{d}} - \mathcal{I}_h \dot{\boldsymbol{d}}\|_{0,\Omega^{\mathrm{s}}} \leq \|\dot{\boldsymbol{d}} - \pi_h^{\mathrm{e}} \dot{\boldsymbol{d}}\|_{0,\Omega^{\mathrm{s}}} + \left(\sum_i \|\alpha_i \boldsymbol{\varphi}_i\|_{0,P_i}^2 \right)^{\frac{1}{2}} \lesssim h^2 |\dot{\boldsymbol{d}}|_{2,\Omega^{\mathrm{s}}} + \left(h^{d-1} \sum_i |\alpha_i|^2 \right)^{\frac{1}{2}}$$

and the result follows using (19).

The estimate for $\|\nabla(\dot{\boldsymbol{d}} - \mathcal{I}_h \dot{\boldsymbol{d}})\|_{0,\Omega^{\mathrm{s}}}$ follows similarly, by using a discrete inverse inequality in P_i.

For the error estimates on the trace Σ, note that we have

$$\|\boldsymbol{\sigma}(\boldsymbol{u} - i_{\mathrm{sz}} E_2 \boldsymbol{u},\, p - i_{\mathrm{sz}} E_1 p)\boldsymbol{n}\|_{-\frac{1}{2},h,\Sigma} \lesssim h^{\frac{1}{2}} \left(\|\nabla(\boldsymbol{u} - i_{\mathrm{sz}} E_2 \boldsymbol{u})\|_{0,\Sigma} + \|p - i_{\mathrm{sz}} E_1 p\|_{0,\Sigma} \right),$$
$$\|(\boldsymbol{u} - i_{\mathrm{sz}} E_2 \boldsymbol{u}) - (\dot{\boldsymbol{d}} - \mathcal{I}_h \dot{\boldsymbol{d}})\|_{\frac{1}{2},h,\Sigma} \lesssim h^{-\frac{1}{2}} (\|\boldsymbol{u} - i_{\mathrm{sz}} E_2 \boldsymbol{u}\|_{0,\Sigma} + \|\dot{\boldsymbol{d}} - \mathcal{I}_h \dot{\boldsymbol{d}}\|_{0,\Sigma}).$$

The quantities on the solid side where the mesh is fitted to interface are treated in a standard fashion using element-wise trace inequalities, followed by approximation in the case of a thick-walled solid and approximation only in the case of a thin-walled solid.

We will detail the estimates for quantities on the unfitted mesh. Using the trace inequality (5) element-wise, for all elements intersected by the interface, we have

$$\begin{aligned} &h^{\frac{1}{2}} \|\nabla(\boldsymbol{u} - i_{\mathrm{sz}} E_2 \boldsymbol{u})\|_{0,\Sigma} + h^{-\frac{1}{2}} \|\boldsymbol{u} - i_{\mathrm{sz}} E_2 \boldsymbol{u}\|_{0,\Sigma} \\ &\quad \lesssim h |E_2 \boldsymbol{u}|_{2,\Omega^{\mathrm{f}}_{\mathcal{T}_h}} + \|\nabla(\boldsymbol{u} - i_{\mathrm{sz}} E_2 \boldsymbol{u})\|_{0,\Omega^{\mathrm{f}}_{\mathcal{T}_h}} + h^{-1} \|\boldsymbol{u} - i_{\mathrm{sz}} E_2 \boldsymbol{u}\|_{0,\Omega^{\mathrm{f}}_{\mathcal{T}_h}} \\ &\quad \lesssim h |E_2 \boldsymbol{u}|_{2,\Omega^{\mathrm{f}}_{\mathcal{T}_h}} \lesssim h |\boldsymbol{u}|_{2,\Omega^{\mathrm{f}}}, \end{aligned}$$

where the last inequality is a consequence of the stability of the extension operator. Similarly we may estimate the trace error of the pressure in the following fashion

$$\begin{aligned} h^{\frac{1}{2}} \|p - i_{\mathrm{sz}} E_1 p\|_{0,\Sigma} &\lesssim h \|\nabla(E_1 p - i_{\mathrm{sz}} E_1 p)\|_{0,\Omega^{\mathrm{f}}_{\mathcal{T}_h}} + \|E_1 p - i_{\mathrm{sz}} E_1 p\|_{0,\Omega^{\mathrm{f}}_{\mathcal{T}}} \\ &\lesssim h |E_1 p|_{1,\Omega^{\mathrm{f}}_{\mathcal{T}_h}} \lesssim h |p|_{1,\Omega^{\mathrm{f}}}, \end{aligned}$$

which concludes the proof. □

By using Lemma 3.1, we get the following energy estimate for the discrete errors $\boldsymbol{\theta}_h,\ y_h,\ \dot{\boldsymbol{\xi}}_h,\ \boldsymbol{\xi}_h$:

$$
\begin{aligned}
&\frac{\rho^{\mathrm{f}}}{2}\|\boldsymbol{\theta}_h(t)\|^2_{0,\Omega^{\mathrm{f}}}+\frac{\rho^{\mathrm{s}}}{2}\|\dot{\boldsymbol{\xi}}_h(t)\|^2_{0,\Omega^{\mathrm{s}}}+\frac{1}{2}\|\boldsymbol{\xi}_h(t)\|^2_{\mathrm{e}}\\
&\quad+c_{\mathrm{s}}\int_0^t\Big[\mu\|\nabla\boldsymbol{\theta}_h\|^2_{0,\Omega^{\mathrm{f}}_{\mathcal{T}_h}}+\gamma\mu\|\boldsymbol{\theta}_h-\dot{\boldsymbol{\xi}}_h\|^2_{\frac{1}{2},h,\Sigma}+|(\boldsymbol{\theta}_h,y_h)|^2_S+a^{\mathrm{e}}(\boldsymbol{\xi}_h,\dot{\boldsymbol{\xi}}_h-\partial_t\boldsymbol{\xi}_h)\Big]\\
&\le\frac{\rho^{\mathrm{f}}}{2}\|\boldsymbol{\theta}_h(0)\|^2_{0,\Omega^{\mathrm{f}}}+\frac{\rho^{\mathrm{s}}}{2}\|\dot{\boldsymbol{\xi}}_h(0)\|^2_{0,\Omega^{\mathrm{s}}}+\frac{1}{2}\|\boldsymbol{\xi}_h(0)\|^2_{\mathrm{e}}\\
&\quad+\int_0^t\Big[\rho^{\mathrm{f}}(\partial_t\boldsymbol{\theta}_h,\boldsymbol{\theta}_h)_{\Omega^{\mathrm{f}}}+\rho^{\mathrm{s}}(\partial_t\dot{\boldsymbol{\xi}}_h,\dot{\boldsymbol{\xi}}_h)_{\Omega^{\mathrm{s}}}+|(\boldsymbol{\theta}_h,y_h)|^2_S+A\big((\boldsymbol{\theta}_h,y_h),(\boldsymbol{\theta}_h,y_h)\big)\\
&\quad-\big(\boldsymbol{\sigma}(\boldsymbol{\theta}_h,y_h)\boldsymbol{n},(\boldsymbol{\theta}_h-\dot{\boldsymbol{\xi}}_h)\big)_{\Sigma}-\big(\boldsymbol{\sigma}(\boldsymbol{\theta}_h,-y_h)\boldsymbol{n},\boldsymbol{\theta}_h-\dot{\boldsymbol{\xi}}_h\big)_{\Sigma}\\
&\quad+\frac{\gamma\mu}{h}\big(\boldsymbol{\theta}_h-\dot{\boldsymbol{\xi}}_h,\boldsymbol{\theta}_h-\dot{\boldsymbol{\xi}}_h\big)_{\Sigma}+a^{\mathrm{e}}(\boldsymbol{\xi}_h,\dot{\boldsymbol{\xi}}_h)\Big].
\end{aligned}
\tag{20}
$$

Observe that due to the different definition of the interpolation operators in $\boldsymbol{\xi}_h$ and $\dot{\boldsymbol{\xi}}_h$, it does not hold that $\dot{\boldsymbol{\xi}}_h=\partial_t\boldsymbol{\xi}_h$. Therefore to obtain the above inequality we used the fact that

$$
\frac{1}{2}\|\boldsymbol{\xi}_h(t)\|^2_{\mathrm{e}}-\frac{1}{2}\|\boldsymbol{\xi}_h(0)\|^2_{\mathrm{e}}+\int_0^t a^{\mathrm{e}}(\boldsymbol{\xi}_h,\dot{\boldsymbol{\xi}}_h-\partial_t\boldsymbol{\xi}_h)=\int_0^t a^{\mathrm{e}}(\boldsymbol{\xi}_h,\dot{\boldsymbol{\xi}}_h).
$$

This results in a non-positive contribution $a^{\mathrm{e}}(\boldsymbol{\xi}_h,\dot{\boldsymbol{\xi}}_h-\partial_t\boldsymbol{\xi}_h)$ in the left-hand side of (20) which will be treated as an approximation error in the error analysis below. Note that the pressure is only controlled in the weak norm given by the stabilization operator.

For the purpose of the analysis, it is convenient to denote the approximation errors by

$$
\begin{aligned}
&\boldsymbol{\theta}_\pi\overset{\mathrm{def}}{=}E_2\boldsymbol{u}-i_{\mathrm{sz}}E_2\boldsymbol{u},\qquad y_\pi\overset{\mathrm{def}}{=}E_1p-i_{\mathrm{sz}}E_1p\quad\text{in }\Omega^{\mathrm{f}}_{\mathcal{T}_h},\\
&\boldsymbol{\xi}_\pi\overset{\mathrm{def}}{=}\boldsymbol{d}-\pi_e\boldsymbol{d},\qquad \dot{\boldsymbol{\xi}}_\pi\overset{\mathrm{def}}{=}\dot{\boldsymbol{d}}-\mathcal{I}_h\dot{\boldsymbol{d}}\quad\text{in }\Omega^{\mathrm{s}}.
\end{aligned}
$$

We are now ready to state and prove our main convergence result.

Theorem 3.1. *Let $(\boldsymbol{u},p,\dot{\boldsymbol{d}},\boldsymbol{d})$ be the solution of (1), (2), (3) or (1), (4) and $(\boldsymbol{u}_h,p_h,\dot{\boldsymbol{d}}_h,\boldsymbol{d}_h)$ be given by (11). Assume that the exact solution $(\boldsymbol{u},p,\dot{\boldsymbol{d}},\boldsymbol{d})$ has the regularity required by the approximation results of Lemma 3.3 and that $\gamma>0$ is given by Lemma 3.1. For $t>0$, there holds:*

$$
\begin{aligned}
&\frac{\rho^{\mathrm{f}}}{2}\|(\boldsymbol{u}_h-\boldsymbol{u})(t)\|^2_{0,\Omega^{\mathrm{f}}}+\frac{\rho^{\mathrm{s}}}{2}\|(\dot{\boldsymbol{d}}_h-\dot{\boldsymbol{d}})(t)\|^2_{0,\Omega^{\mathrm{s}}}+\frac{1}{2}\|(\boldsymbol{d}_h-\boldsymbol{d})(t)\|^2_{\mathrm{e}}\\
&\quad+c_{\mathrm{s}}\int_0^t\Big[\mu\|\nabla(\boldsymbol{u}_h-\boldsymbol{u})\|^2_{0,\Omega^{\mathrm{f}}}+\gamma\mu\|\boldsymbol{u}_h-\dot{\boldsymbol{d}}_h\|^2_{\frac{1}{2},h,\Sigma}\Big]\lesssim h^2.
\end{aligned}
$$

Proof. By a triangle inequality and the optimal approximability of the proposed interpolants it is sufficient to prove the convergence of the discrete error $(\boldsymbol{\theta}_h,y_h,\dot{\boldsymbol{\xi}}_h,\boldsymbol{\xi}_h)$. Consider first the inequality (20). After applying the Galerkin orthogonality (14) in the right-hand side and noting that by the definition of π^{e}_h, $a^{\mathrm{e}}(\boldsymbol{\xi}_\pi,\dot{\boldsymbol{\xi}}_h)=0$, we have

$$
\begin{aligned}
&\frac{\rho^{\mathrm{f}}}{2}\|\boldsymbol{\theta}_h(t)\|^2_{0,\Omega^{\mathrm{f}}}+\frac{\rho^{\mathrm{s}}}{2}\|\dot{\boldsymbol{\xi}}_h(t)\|^2_{0,\Omega^{\mathrm{s}}}+\frac{1}{2}\|\boldsymbol{\xi}_h(t)\|^2_{\mathrm{e}}\\
&\quad+c_{\mathrm{s}}\int_0^t\Big[\mu\|\nabla\boldsymbol{\theta}_h\|^2_{0,\Omega^{\mathrm{f}}_{\mathcal{T}}}+\gamma\mu\|\boldsymbol{\theta}_h-\dot{\boldsymbol{\xi}}_h\|^2_{\frac{1}{2},h,\Sigma}+|(\boldsymbol{\theta}_h,y_h)|^2_S\Big]\\
&\le\frac{\rho^{\mathrm{f}}}{2}\|\boldsymbol{\theta}_h(0)\|^2_{0,\Omega^{\mathrm{f}}}+\frac{\rho^{\mathrm{s}}}{2}\|\dot{\boldsymbol{\xi}}_h(0)\|^2_{0,\Omega^{\mathrm{s}}}+\frac{1}{2}\|\boldsymbol{\xi}_h(0)\|^2_{\mathrm{e}}\\
&\quad+\int_0^t\Big[\underbrace{(\partial_t\boldsymbol{\theta}_\pi,\boldsymbol{\theta}_h)_{\Omega^{\mathrm{f}}}+(\partial_t\dot{\boldsymbol{\xi}}_\pi,\dot{\boldsymbol{\xi}}_h)}_{T_1}+\underbrace{S_h\big((i_{\mathrm{sz}}E_2\boldsymbol{u}(t),i_{\mathrm{sz}}E_1p(t)),(\boldsymbol{\theta}_h,y_h)\big)}_{T_2}
\end{aligned}
$$

$$\times \underbrace{A\big((\boldsymbol{\theta}_\pi, y_\pi), (\boldsymbol{\theta}_h, y_h)\big) - \big(\boldsymbol{\sigma}(\boldsymbol{\theta}_\pi, y_\pi)\boldsymbol{n}, (\boldsymbol{\theta}_h - \dot{\boldsymbol{\xi}}_h)\big)_\Sigma - \big(\boldsymbol{\sigma}(\boldsymbol{\theta}_h, y_h)\boldsymbol{n}, \boldsymbol{\theta}_\pi - \dot{\boldsymbol{\xi}}_\pi\big)_\Sigma}_{T_3}$$

$$+ \underbrace{\frac{\gamma\mu}{h}\big(\boldsymbol{\theta}_\pi - \dot{\boldsymbol{\xi}}_\pi, \boldsymbol{\theta}_h - \dot{\boldsymbol{\xi}}_h\big)_\Sigma}_{T_4} - \underbrace{a^{\mathrm{e}}(\boldsymbol{\xi}_h, \dot{\boldsymbol{\xi}}_h - \partial_t\boldsymbol{\xi}_h)}_{T_5}\Big]. \tag{21}$$

We may now bound the terms $T_1, \dots, T_5$ term by term. Mainly by applying Cauchy–Schwarz inequality followed by trace inequalities and approximation. For the first term we have

$$\begin{aligned}\int_0^t T_1 &\le \rho^{\mathrm{f}}\|\partial_t\boldsymbol{\theta}_\pi\|_{L^2(0,t;\Omega^{\mathrm{f}})}\|\boldsymbol{\theta}_h\|_{L^2(0,t;\Omega^{\mathrm{f}})} + \|\partial_t\dot{\boldsymbol{\xi}}_\pi\|_{L^2(0,t;\Omega^{\mathrm{f}})}\|\dot{\boldsymbol{\xi}}_h\|_{L^2(0,t;\Omega^{\mathrm{s}})}\\ &\le Ch^4(\rho^{\mathrm{f}}\|\partial_t\boldsymbol{u}\|^2_{L^2(0,t;H^2(\Omega^{\mathrm{f}}))} + \rho^{\mathrm{s}}\|\partial_t\dot{\boldsymbol{d}}\|^2_{L^2(0,t;H^2(\Omega^{\mathrm{s}}))}) + \rho^{\mathrm{f}}\|\boldsymbol{\theta}_h\|^2_{L^2(0,t;\Omega^{\mathrm{f}})} + \rho^{\mathrm{s}}\|\dot{\boldsymbol{\xi}}_h\|^2_{L^2(0,t;\Omega^{\mathrm{s}})}.\end{aligned}$$

The two first terms in the right-hand side have optimal convergence order and the last two may be controlled using Gronwall's lemma.

For T_2 we observe that

$$\int_0^t T_2 \le \frac{1}{2c_{\mathrm{s}}}\int_0^t |i_{\mathrm{sz}}E_2\boldsymbol{u}(t), i_{\mathrm{sz}}E_1 p(t)|_S^2 + \frac{c_{\mathrm{s}}}{2}\int_0^t |(\boldsymbol{\theta}_h, y_h)|_S^2,$$

where the second term in the right-hand side is absorbed in the left-hand side of (21) and the first term is bounded using the approximation (16).

To estimate T_3 we first note that the second term in the expression is bounded by the Cauchy–Schwarz inequality followed by approximation

$$\begin{aligned}\int_0^t |\big(\boldsymbol{\sigma}(\boldsymbol{\theta}_\pi, y_\pi)\boldsymbol{n}, (\boldsymbol{\theta}_h - \dot{\boldsymbol{\xi}}_h)\big)_\Sigma| &\le Ch^2(|\boldsymbol{u}|^2_{L^2(0,t;H^2(\Omega^{\mathrm{f}}))} + |p|^2_{L^2(0,t;H^1(\Omega^{\mathrm{f}}))})\\ &\quad + \frac{c_{\mathrm{s}}}{4}\gamma\mu\int_0^t \|\boldsymbol{\theta}_h - \dot{\boldsymbol{\xi}}_h\|^2_{\frac{1}{2},h,\Sigma}.\end{aligned} \tag{22}$$

We then consider the velocity part and observe that

$$\begin{aligned}\int_0^t (a(\boldsymbol{\theta}_\pi, \boldsymbol{\theta}_h) - \big(\boldsymbol{\sigma}(\boldsymbol{\theta}_h, 0)\boldsymbol{n}, \boldsymbol{\theta}_\pi - \dot{\boldsymbol{\xi}}_\pi\big)_\Sigma) &\le Ch^2(\|\boldsymbol{u}\|^2_{L^2(0,t;H^2(\Omega^{\mathrm{f}}))} + \|\dot{\boldsymbol{d}}\|^2_{L^2(0,t;H^2(\Omega^{\mathrm{s}}))})\\ &\quad + \frac{c_{\mathrm{s}}}{2}\mu\int_0^t \|\nabla\boldsymbol{\theta}_h\|^2_{0,\Omega^{\mathrm{f}}_{\mathcal{T}}}.\end{aligned} \tag{23}$$

The pressure velocity coupling is the most interesting part of the continuity. For the remaining terms of T_3 we write, using an integration by parts in the mass conservation equation,

$$\begin{aligned}&b(y_\pi, \boldsymbol{\theta}_h) - b(y_h, \boldsymbol{\theta}_\pi) - \big(\boldsymbol{\sigma}(0, -y_h)\boldsymbol{n}, \boldsymbol{\theta}_\pi - \dot{\boldsymbol{\xi}}_\pi\big)_\Sigma\\ &\quad = (y_\pi, \nabla\cdot\boldsymbol{\theta}_h)_{\Omega^{\mathrm{f}}} - (y_h, \nabla\cdot\boldsymbol{\theta}_\pi)_{\Omega^{\mathrm{f}}} - \big(\boldsymbol{\sigma}(0, -y_h)\boldsymbol{n}, \boldsymbol{\theta}_\pi - \dot{\boldsymbol{\xi}}_\pi\big)_\Sigma\\ &\quad = \underbrace{(y_\pi, \nabla\cdot\boldsymbol{\theta}_h)_{\Omega^{\mathrm{f}}}}_{T_{31}} - \underbrace{(\nabla y_h, \boldsymbol{\theta}_\pi)_{\Omega^{\mathrm{f}}}}_{T_{32}} - \underbrace{\big(\boldsymbol{\sigma}(0, y_h)\boldsymbol{n}, \dot{\boldsymbol{\xi}}_\pi\big)_\Sigma}_{T_{33}}.\end{aligned} \tag{24}$$

Estimating the terms T_{31} and T_{32} we get

$$\begin{aligned}\int_0^t T_{31} &\le Ch^2|p|^2_{L^2(0,t;H^1(\Omega^{\mathrm{f}}))} + \frac{c_{\mathrm{s}}}{4}\mu\int_0^t \|\nabla\boldsymbol{\theta}_h\|^2_{0,\Omega^{\mathrm{f}}},\\ \int_0^t T_{32} &\le Ch^2\|\boldsymbol{u}\|^2_{L^2(0,t;H^2(\Omega^{\mathrm{f}}))} + \frac{c_{\mathrm{s}}}{8}\int_0^t |(0, y_h)|_S^2.\end{aligned}$$

Denoting by y_i the average of y_h over the interface patch F_i we obtain, using the property (15) of the interpolant $\mathcal{I}_h$,

$$\begin{aligned}T_{33} &= \sum_i \inf_{y_i\in\mathbb{R}}\big(y_h - y_i, \dot{\boldsymbol{\xi}}_\pi\cdot\boldsymbol{n}\big)_{F_i} \le C\|h\nabla y_h\|_{0,\Omega^{\mathrm{f}}_{\mathcal{T}_h}} h|\dot{\boldsymbol{d}}|_{2,\Omega^{\mathrm{s}}}\\ &\le \frac{c_{\mathrm{s}}}{8}|(0, y_h)|_S^2 + Ch^2|\dot{\boldsymbol{d}}|^2_{2,\Omega^{\mathrm{s}}}.\end{aligned} \tag{25}$$

The boundary penalty term T_4 is handled using the Cauchy–Schwarz inequality followed by approximation,

$$\begin{aligned}\int_0^t T_4 &\le \frac{1}{c_s}\gamma\mu\int_0^t \|\boldsymbol{\theta}_\pi - \dot{\boldsymbol{\xi}}_\pi\|^2_{\frac{1}{2},h,\Sigma} + \frac{c_s}{4}\gamma\mu\int_0^t \|\boldsymbol{\theta}_h - \dot{\boldsymbol{\xi}}_h\|^2_{\frac{1}{2},h,\Sigma}\\ &\le \frac{1}{c_s}\gamma\mu h^2(\|\boldsymbol{u}\|^2_{L^2(0,t;H^2(\Omega^f))} + \|\dot{\boldsymbol{d}}\|^2_{L^2(0,t;H^2(\Omega^s))}) + \frac{c_s}{4}\gamma\mu\int_0^t \|\boldsymbol{\theta}_h - \dot{\boldsymbol{\xi}}_h\|^2_{\frac{1}{2},h,\Sigma}. \end{aligned} \tag{26}$$

Note that the first term has the right convergence order and the second term can be absorbed in the left-hand side of (21).

Finally, term T_5 is bounded using the fact that $\dot{\boldsymbol{\xi}}_h - \partial_t\boldsymbol{\xi}_h = \sum_i \alpha_i\boldsymbol{\varphi}_i$ and the convergence order of the perturbation is known (cf., the bound (17)),

$$\begin{aligned}\int_0^t T_5 &= \int_0^t a^e(\boldsymbol{\xi}_h, \dot{\boldsymbol{\xi}}_h - \partial_t\boldsymbol{\xi}_h) = \sum_i\int_0^t a^e(\boldsymbol{\xi}_h, \alpha_i\boldsymbol{\varphi}_i)\\ &\le \sum_i\int_0^t \|\boldsymbol{\xi}_h\|_e\|\alpha_i\boldsymbol{\varphi}_i\|_{1,\Omega^s} \lesssim \int_0^t \|\boldsymbol{\xi}_h\|^2_e + h^2\|\dot{\boldsymbol{d}}\|^2_{L^2(0,t;H^2(\Omega^s))}.\end{aligned}$$

We may now collect the above bounds to obtain the bound

$$\begin{aligned}&\frac{\rho^f}{2}\|\boldsymbol{\theta}_h(t)\|^2_{0,\Omega^f} + \frac{\rho^s}{2}\|\dot{\boldsymbol{\xi}}_h(t)\|^2_{0,\Omega^s} + \frac{1}{2}\|\boldsymbol{\xi}_h(t)\|^2_e\\ &\quad + \frac{c_s}{4}\int_0^t\Big[\mu_f\|\nabla\boldsymbol{\theta}_h\|^2_{0,\Omega^f_{\mathcal{I}}} + \gamma\mu\|\boldsymbol{\theta}_h - \dot{\boldsymbol{\xi}}_h\|^2_{\frac{1}{2},h,\Sigma} + |(\boldsymbol{\theta}_h, y_h)|^2_S\Big]\\ &\le \frac{\rho^f}{2}\|\boldsymbol{\theta}_h(0)\|^2_{0,\Omega^f} + \frac{\rho^s}{2}\|\dot{\boldsymbol{\xi}}_h(0)\|^2_{0,\Omega^s} + \frac{1}{2}\|\boldsymbol{\xi}_h(0)\|^2_e\\ &\quad + Cth^4\left(\rho^f\|\partial_t\boldsymbol{u}\|^2_{L^2(0,t;H^2(\Omega^f))} + \rho^s\|\partial_t\dot{\boldsymbol{d}}\|^2_{L^2(0,t;H^2(\Omega^s))}\right)\\ &\quad + Cth^2\left(|\boldsymbol{u}|^2_{L^2(0,t;H^2(\Omega^f))} + |p|^2_{L^2(0,t;H^1(\Omega^f))} + \|\dot{\boldsymbol{d}}\|^2_{L^2(0,t;H^2(\Omega^s))}\right)\\ &\quad + t^{-1}\left(\rho^f\|\boldsymbol{\theta}_h\|^2_{L^2(0,t;\Omega^f)} + \rho^s\|\dot{\boldsymbol{\xi}}_h\|^2_{L^2(0,t;\Omega^s)} + \int_0^t\|\boldsymbol{\xi}_h\|^2_e\right).\end{aligned}$$

We conclude the proof by applying Gronwall's lemma. □

4. Time discretization: coupling schemes

This section is devoted to the time discretization of the space semi-discrete formulation (11). Both implicit and explicit coupling strategies are discussed. In the subsequent text, the parameter $\tau > 0$ stands for the time-step length, $t_n \overset{\text{def}}{=} n\tau$, for $n \in \mathbb{N}$ and $\partial_\tau x^n \overset{\text{def}}{=} (x^n - x^{n-1})/\tau$ for the first-order backward difference. We also introduce the fluid discrete bi-linear form

$$a^f_h\big((\boldsymbol{u}_h, p_h), (\boldsymbol{v}_h, q_h)\big) \overset{\text{def}}{=} A\big((\boldsymbol{u}_h, p_h), (\boldsymbol{v}_h, q_h)\big) + S_h\big((\boldsymbol{u}_h, p_h), (\boldsymbol{v}_h, q_h)\big).$$

4.1. Implicit coupling

An overall implicit first-order scheme is considered for the time-discretization of (11). This yields the time-advancing procedure reported in Algorithm 1.

Note that at each time level n, the fluid $(\boldsymbol{u}^n_h, p^n_h)$ and solid $(\dot{\boldsymbol{d}}^n_h, \boldsymbol{d}^n_h)$ states are fully coupled. The next result states the unconditional stability of the implicit scheme given by (27), and where

$$E^n \overset{\text{def}}{=} \frac{\rho^f}{2}\|\boldsymbol{u}^n_h\|^2_{0,\Omega^f} + \frac{\rho^s}{2}\|\dot{\boldsymbol{d}}^n_h\|^2_{0,\Omega^s} + a^e(\boldsymbol{d}^n_h, \boldsymbol{d}^n_h),$$

denotes the total energy of the discrete system a time t_n.

Algorithm 1 Implicit coupling scheme

For $n \geq 1$, find $\left(\boldsymbol{u}_h^n, p_h^n, \dot{\boldsymbol{d}}_h^n, \boldsymbol{d}_h^n\right) \in \boldsymbol{V}_h \times Q_h \times \boldsymbol{W}_h \times \boldsymbol{W}_h$, such that $\dot{\boldsymbol{d}}_h = \partial_\tau \boldsymbol{d}_h^n$ and

$$\begin{cases} \rho^{\mathrm{f}}\left(\partial_\tau \boldsymbol{u}_h^n, \boldsymbol{v}_h\right) + a_h^{\mathrm{f}}\left((\boldsymbol{u}_h^n, p_h^n), (\boldsymbol{v}_h, q_h)\right) + \rho^{\mathrm{s}}\left(\partial_\tau \dot{\boldsymbol{d}}_h^n, \boldsymbol{w}_h\right)_{\Omega^{\mathrm{s}}} + a^{\mathrm{e}}(\boldsymbol{d}_h^n, \boldsymbol{w}_h) \\ \quad - \left(\boldsymbol{\sigma}(\boldsymbol{u}_h^n, p_h^n)\boldsymbol{n}, (\boldsymbol{v}_h - \boldsymbol{w}_h)\right)_\Sigma - \left((\boldsymbol{u}_h^n - \dot{\boldsymbol{d}}_h^n), \boldsymbol{\sigma}(\boldsymbol{v}_h, -q_h)\boldsymbol{n}\right)_\Sigma \\ \quad + \dfrac{\gamma\mu}{h}\left((\boldsymbol{u}_h^n - \dot{\boldsymbol{d}}_h^n), (\boldsymbol{v}_h - \boldsymbol{w}_h)\right)_\Sigma = 0 \end{cases} \tag{27}$$

for all $(\boldsymbol{v}_h, q_h, \boldsymbol{w}_h) \in \boldsymbol{V}_h \times Q_h \times \boldsymbol{W}_h$.

Lemma 4.1. *Let $\{(\boldsymbol{u}_h^n, p_h^n, \dot{\boldsymbol{d}}_h^n, \boldsymbol{d}_h^n)\}_{n\geq 1}$ be the sequence given by Algorithm* 1. *Then, under the condition $C_{\mathrm{TI}}^2 \lesssim \gamma$, there holds $E^n \leq E^0$ for all $n \geq 1$.*

Proof. The result is a straightforward consequence of Lemma 3.1, after taking $(\boldsymbol{v}_h, q_h, \boldsymbol{w}_h) = (\boldsymbol{u}_h^n, p_h^n, \dot{\boldsymbol{d}}_h^n)$ in (27). □

4.2. Explicit coupling

In this paragraph we introduce time-marching procedures that allow an uncoupled computation of the fluid $(\boldsymbol{u}_h^n, p_h^n)$ and solid $(\dot{\boldsymbol{d}}_h^n, \boldsymbol{d}_h^n)$ states (explicit coupling schemes). Basically, the proposed methods generalized the Nitsche-based splitting schemes, introduced in [6,7], to the unfitted framework provided by (11). To this purpose, we first note that the monolithic problem (11) can be equivalently formulated in terms of two coupled sub-problems: for $t > 0$

- Solid sub-problem: find $\left(\dot{\boldsymbol{d}}_h(t), \boldsymbol{d}_h(t)\right) \in \boldsymbol{W}_h \times \boldsymbol{W}_h$ with $\dot{\boldsymbol{d}}_h(t) = \partial_t \boldsymbol{d}_h(t)$ and such that

$$\rho^{\mathrm{s}}\left(\partial_t \dot{\boldsymbol{d}}_h, \boldsymbol{w}_h\right)_{\Omega^{\mathrm{s}}} + a^{\mathrm{e}}(\boldsymbol{d}_h, \boldsymbol{w}_h) + \frac{\gamma\mu}{h}\left(\dot{\boldsymbol{d}}_h, \boldsymbol{w}_h\right)_\Sigma = -\frac{\gamma\mu}{h}\left(\boldsymbol{u}_h, \boldsymbol{w}_h\right)_\Sigma - \left(\boldsymbol{\sigma}(\boldsymbol{u}_h, p_h)\boldsymbol{n}, \boldsymbol{w}_h\right)_\Sigma \tag{28}$$

  for all $\boldsymbol{w}_h \in \boldsymbol{W}_h$.
- Fluid sub-problem: find $(\boldsymbol{u}_h(t), p_h(t)) \in \boldsymbol{V}_h \times Q_h$ such that

$$\begin{aligned} &\rho^{\mathrm{f}}\left(\partial_t \boldsymbol{u}_h, \boldsymbol{v}_h\right)_{\Omega^{\mathrm{f}}} + a_h^{\mathrm{f}}\left((\boldsymbol{u}_h, p_h), (\boldsymbol{v}_h, q_h)\right) - \left((\boldsymbol{u}_h - \dot{\boldsymbol{d}}_h), \boldsymbol{\sigma}(\boldsymbol{v}_h, -q_h)\boldsymbol{n}\right)_\Sigma \\ &\quad + \frac{\gamma\mu}{h}\left(\boldsymbol{u}_h, \boldsymbol{v}_h\right)_\Sigma = \frac{\gamma\mu}{h}\left(\dot{\boldsymbol{d}}_h, \boldsymbol{v}_h\right)_\Sigma + \left(\boldsymbol{\sigma}(\boldsymbol{u}_h, p_h)\boldsymbol{n}, \boldsymbol{v}_h\right)_\Sigma \end{aligned} \tag{29}$$

  for all $(\boldsymbol{v}_h, q_h) \in \boldsymbol{V}_h \times Q_h$.

Algorithm 2 Stabilized explicit coupling scheme

For $n \geq 1$:

1. Solid sub-step: find $\left(\dot{\boldsymbol{d}}_h^n, \boldsymbol{d}_h^n\right) \in \boldsymbol{W}_h \times \boldsymbol{W}_h$ with $\dot{\boldsymbol{d}}_h^n = \partial_\tau \boldsymbol{d}_h^n$ and such that

$$\begin{aligned} &\rho^{\mathrm{s}}\left(\partial_\tau \dot{\boldsymbol{d}}_h^n, \boldsymbol{w}_h\right)_{\Omega^{\mathrm{s}}} + a^{\mathrm{e}}(\boldsymbol{d}_h^n, \boldsymbol{w}_h) + \frac{\gamma\mu}{h}\left(\dot{\boldsymbol{d}}_h^n, \boldsymbol{w}_h\right)_\Sigma \\ &\qquad = -\frac{\gamma\mu}{h}\left(\boldsymbol{u}_h^{n-1}, \boldsymbol{w}_h\right)_\Sigma - \left(\boldsymbol{\sigma}(\boldsymbol{u}_h^{n-1}, p_h^{n-1})\boldsymbol{n}, \boldsymbol{w}_h\right)_\Sigma \end{aligned} \tag{30}$$

   for all $\boldsymbol{w}_h \in \boldsymbol{W}_h$.
2. Fluid sub-step: find $(\boldsymbol{u}_h^n, p_h^n) \in \boldsymbol{V}_h \times Q_h$ such that

$$\begin{aligned} &\rho^{\mathrm{f}}\left(\partial_\tau \boldsymbol{u}_h^n, \boldsymbol{v}_h\right)_{\Omega^{\mathrm{f}}} + a_h^{\mathrm{f}}\left((\boldsymbol{u}_h^n, p_h^n), (\boldsymbol{v}_h, q_h)\right) - \left(\boldsymbol{u}_h^n - \dot{\boldsymbol{d}}_h^n, q_h\boldsymbol{n}\right)_\Sigma + \frac{\gamma\mu}{h}\left(\boldsymbol{u}_h^n, \boldsymbol{v}_h\right)_\Sigma \\ &\quad + \frac{\gamma_0 h}{\gamma\mu}\left(p_h^n - p_h^{n-1}, q_h\right)_\Sigma = \frac{\gamma\mu}{h}\left(\dot{\boldsymbol{d}}_h^n, \boldsymbol{v}_h\right)_\Sigma + \left(\boldsymbol{\sigma}(\boldsymbol{u}_h^{n-1}, p_h^{n-1})\boldsymbol{n}, \boldsymbol{v}_h\right)_\Sigma \end{aligned} \tag{31}$$

   for all $(\boldsymbol{v}_h, q_h) \in \boldsymbol{V}_h \times Q_h$.

Following [6,7], we propose to uncouple the time-marching of (28) and (29) through the explicit treatment of the interface fluid terms in (28), as detailed in Algorithm 2. Note that, in the fluid sub-step (31), the interface fluid stress

is explicitly treated. This explains why the symmetrizing viscous term

$$\big((\boldsymbol{u}_h^n - \dot{\boldsymbol{d}}_h^n), \boldsymbol{\sigma}(\boldsymbol{v}_h, 0)\boldsymbol{n}\big)_\Sigma,$$

is missing in (31). The weakly consistent interface pressure stabilization,

$$\frac{\gamma_0 h}{\gamma\mu}\big(p_h^n - p_h^{n-1}, q_h\big)_\Sigma, \quad \gamma_0 > 0,$$

is introduced to control the artificial interface pressure fluctuations induced by the splitting of pressure stress in time.

Algorithm 3 Stabilized explicit coupling scheme with K-correction steps

For $n \geq 2$:

1. Extrapolation:

$$\boldsymbol{u}_h^{n,0} = 2\boldsymbol{u}_h^{n-1} - \boldsymbol{u}_h^{n-2}, \quad \boldsymbol{\sigma}(\boldsymbol{u}_h^{n,0}, p_h^{n,0})\boldsymbol{n} = \boldsymbol{\sigma}(\boldsymbol{u}_h^{n-1}, p_h^{n-1})\boldsymbol{n}, \quad p_h^{n,0} = p_h^{n-1}. \tag{32}$$

2. For $k = 1, \ldots, K+1$:
   - Solid sub-step: find $\big(\dot{\boldsymbol{d}}_h^{n,k}, \boldsymbol{d}_h^{n,k}\big) \in \boldsymbol{W}_h \times \boldsymbol{W}_h$, with $\dot{\boldsymbol{d}}_h^{n,k} = (\boldsymbol{d}_h^{n,k} - \dot{\boldsymbol{d}}_h^{n-1})/\tau$ and such that
   $$\rho^{\mathrm{s}}\big(\partial_\tau \dot{\boldsymbol{d}}_h^{n,k}, \boldsymbol{w}_h\big)_{\Omega^{\mathrm{s}}} + a^{\mathrm{e}}(\boldsymbol{d}_h^{n,k}, \boldsymbol{w}_h) + \frac{\gamma\mu}{h}\big(\dot{\boldsymbol{d}}_h^{n,k}, \boldsymbol{w}_h\big)_\Sigma$$
   $$= -\frac{\gamma\mu}{h}\big(\boldsymbol{u}_h^{n,k-1}, \boldsymbol{w}_h\big)_\Sigma - \big(\boldsymbol{\sigma}(\boldsymbol{u}_h^{n,k-1}, p_h^{n,k-1})\boldsymbol{n}, \boldsymbol{w}_h\big)_\Sigma$$
   for all $\boldsymbol{w}_h \in \boldsymbol{W}_h$.
   - Fluid sub-step: find $(\boldsymbol{u}_h^{n,k}, p_h^{n,k}) \in \boldsymbol{V}_h \times Q_h$ such that
   $$\rho^{\mathrm{f}}\big(\partial_\tau \boldsymbol{u}_h^{n,k}, \boldsymbol{v}_h\big)_{\Omega^{\mathrm{f}}} + a_h^{\mathrm{f}}\big((\boldsymbol{u}_h^{n,k}, p_h^{n,k}), (\boldsymbol{v}_h, q_h)\big) - \big(\boldsymbol{u}_h^n - \dot{\boldsymbol{d}}_h^{n,k}, q_h\boldsymbol{n}\big)_\Sigma + \frac{\gamma\mu}{h}\big(\boldsymbol{u}_h^{n,k}, \boldsymbol{v}_h\big)_\Sigma$$
   $$+\frac{\gamma_0 h}{\gamma\mu}\big(p_h^{n,k} - p_h^{n,k-1}, q_h\big)_\Sigma \quad = \frac{\gamma\mu}{h}\big(\dot{\boldsymbol{d}}_h^{n,k}, \boldsymbol{v}_h\big)_\Sigma + \big(\boldsymbol{\sigma}(\boldsymbol{u}_h^{n,k-1}, p_h^{n,k-1})\boldsymbol{n}, \boldsymbol{v}_h\big)_\Sigma$$
   for all $(\boldsymbol{v}_h, q_h) \in \boldsymbol{V}_h \times Q_h$.
3. Solution update:

$$\boldsymbol{u}_h^n = \boldsymbol{u}_h^{n,K+1}, \quad p_h^n = p_h^{n,K+1}, \quad \dot{\boldsymbol{d}}_h^n = \dot{\boldsymbol{d}}_h^{n,K+1}, \quad \boldsymbol{d}_h^n = \boldsymbol{d}_h^{n,K+1}.$$

The next result guarantees the conditional stability of Algorithm 2.

Lemma 4.2. *Let $\{(\boldsymbol{u}_h^n, p_h^n, \dot{\boldsymbol{d}}_h^n, \boldsymbol{d}_h^n)\}_{n\geq 1}$ be the sequence given by Algorithm 2. Then, under the following conditions,*

$$C_{\mathrm{TI}}^2 \lesssim \gamma, \qquad \gamma\tau \lesssim h, \qquad 1 \lesssim \gamma_0,$$
$$E^n \lesssim E^0 + \mu\|\boldsymbol{u}_h^0\|_{0,\Sigma}^2 + \mu\|\boldsymbol{\epsilon}(\boldsymbol{u}_h^0)\|_{0,\Omega_{\mathrm{f}}}^2 + \frac{\gamma_0 h}{\gamma\mu}\tau\|p_h^0\|_{0,\Sigma}^2$$

for $n \geq 1$.

Proof. The result follows by combining Lemma 3.1 with the arguments reported in [6, Section 5.1]. □

The main drawback of Algorithm 2 is its poor accuracy compared to Algorithm 1. In fact, the interface time splitting introduces a truncation error whose leading contribution is of the form $\mathcal{O}(\tau/h)$, which prevents convergence under the stability conditions of Lemma 4.2. This error perturbation comes from explicit treatment of the penalty term in the right-hand side of (30). In order to retain overall first-order accuracy under the standard condition $\tau = \mathcal{O}(h)$ imposed by the stability, we propose to combine Algorithm 2 with an extrapolation/correction strategy (see [7, Section 4.1]).

The resulting procedure is detailed in Algorithm 3, where $K \geq 0$ indicates the number of correction steps. Here, we have used the notation $\partial_\tau x^{n,k} = (x^{n,k} - x^{n-1})/\tau$. The purpose of the second-order extrapolation, in (32), is to retrieve a truncation error in the penalty term of the form $\mathcal{O}\big((\tau^2/h)^{K+1}\big)$, after K-correction iterations. Note that without any correction, ($K = 0$), this contribution is $\mathcal{O}\big((\tau^2/h)\big)$ and hence an overall $\mathcal{O}(h)$ is expected under $\tau = \mathcal{O}(h)$. Numerical evidence shows, however, that $K \geq 1$ is required for stability.

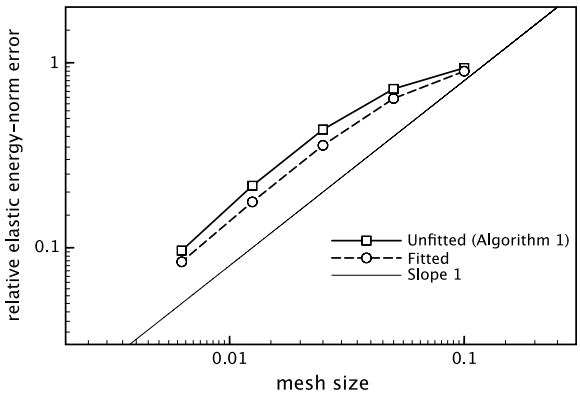

Fig. 2. Unfitted vs. fitted methods. Convergence history of the displacement at time $t = 0.015$. Space–time grid refinement under $\tau = \mathcal{O}(h)$.

5. Numerical example

In order to illustrate the accuracy and performance of the proposed schemes, we consider the widespread two-dimensional pressure-wave propagation benchmark (see, e.g., [26]). The fluid domain and the fluid–solid interface are, respectively, $\Omega^{\mathrm{f}} = (0, L) \times (0, R)$, $\Sigma = [0, L] \times \{R\}$, with $L = 6$ and $R = 0.5$. A generalized string model is taken for the structure. Hence $\overline{\Omega^{\mathrm{s}}} = \Sigma$ and in (4) we take

$$\boldsymbol{d} = \begin{pmatrix} 0 \\ \eta \end{pmatrix}, \qquad \boldsymbol{L}^{\mathrm{e}}\boldsymbol{d} = \begin{pmatrix} 0 \\ -\lambda_1 \partial_{xx}\eta + \lambda_0 \eta \end{pmatrix}, \qquad \lambda_1 \stackrel{\mathrm{def}}{=} \frac{E\epsilon}{2(1+\nu)}, \qquad \lambda_0 \stackrel{\mathrm{def}}{=} \frac{E\epsilon}{R^2(1-\nu^2)}.$$

Then the elastic bi-linear form reads

$$a^{\mathrm{e}}(\boldsymbol{d}, \boldsymbol{w}) \stackrel{\mathrm{def}}{=} \lambda_1(\partial_x \eta, \partial_x w)_\Sigma + \lambda_0(\eta, w)_\Sigma,$$

with $\boldsymbol{w} = (0, w)^{\mathrm{T}}$. As usual, here E denotes the Young modulus and ν the Poisson ratio of the solid. All the quantities will be given in the CGS system. At $x = 0$ we impose a sinusoidal pressure of maximal amplitude 2×10^4 during $5 \cdot 10^{-3}$ s, corresponding to half a period. Zero pressure is enforced at $x = 6$ and a symmetry condition is applied on the lower wall $y = 0$. The solid is clamped at its extremities, $x = 0, L$. The fluid physical parameters are given by $\rho^{\mathrm{f}} = 1.0$, $\mu = 0.035$, while for the solid we have $\rho^{\mathrm{s}} = 1.1$, $\epsilon = 0.1$, $E = 0.75 \times 10^6$ and $\nu = 0.5$.

Fig. 5 shows an example of unfitted and fitted fluid computational meshes considered in the computations. In the unfitted case, we have $\Omega^{\mathrm{f}}_{\mathcal{T}_h} = [0, 6] \times [0, 0.8]$ and hence $\overline{\Omega^{\mathrm{f}}} \subset \Omega^{\mathrm{f}}_{\mathcal{T}_h}$. The ghost-penalty stabilization bi-linear form in (10) has been defined on the whole computational domain, that is,

$$g_h(\boldsymbol{u}_h, \boldsymbol{v}_h) \stackrel{\mathrm{def}}{=} \gamma_{\mathrm{g}} \sum_{K \in \mathcal{T}_h^{\mathrm{f}}} \int_{\partial K \setminus \partial \Omega^{\mathrm{f}}_{\mathcal{T}_h}} \mu h [\![\nabla \boldsymbol{u}_h]\!]_{\partial K} \cdot [\![\nabla \boldsymbol{v}_h]\!]_{\partial K},$$

where the symbol $[\![\cdot]\!]_F$ denotes the jump of given quantity across the edge or face F. The free stabilization parameters have been set to $\gamma = 1000$, $\gamma_{\mathrm{g}} = 1$ and $\gamma_{\mathrm{p}} = 10^{-3}$ (in (8)). All the computations have been performed with FreeFem++ [27].

In Fig. 6 we have reported a few snapshots of the pressure field obtained with Algorithm 1, taking $\tau = 2 \cdot 10^{-4}$ and $h = 0.1$. The numerical solution remains stable, as predicted by Lemma 4.1, and a propagating pressure-wave is observed. For comparison purposes, Fig. 7 reports the snapshots of the pressure obtained with a fitted method and interface matching discretizations. The good agreement of the two numerical solutions in the physical domain Ω^{f} is clearly visible. Similar conclusions can be inferred from Fig. 8, which reports the corresponding interface displacements at $t = 0.015$. The depicted reference solution has been generated using the fitted method with a high space–time grid resolution ($h = 3.125 \times 10^{-3}$, $\tau = 10^{-6}$).

In order to highlight the overall accuracy of Algorithm 1, we have refined both in time and in space at the same rate, $\tau = \mathcal{O}(h)$, with the following set of discrete parameters:

$$(\tau, h) \in \left\{ 2^{-i} \left(2 \cdot 10^{-4}, 0.1 \right) \right\}_{i=0}^{4}. \tag{33}$$

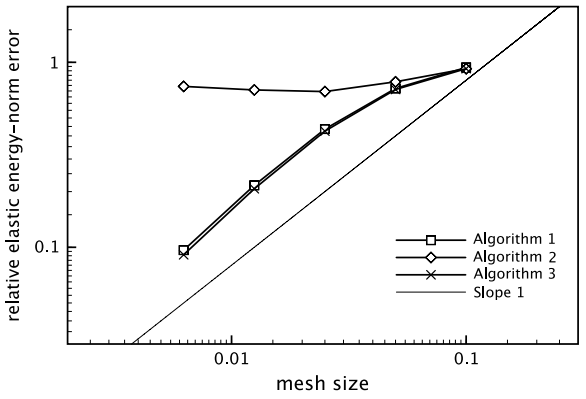

Fig. 3. Implicit vs. explicit coupling. Convergence history of the displacement at time $t = 0.015$. Space–time grid refinement under $\tau = \mathcal{O}(h)$.

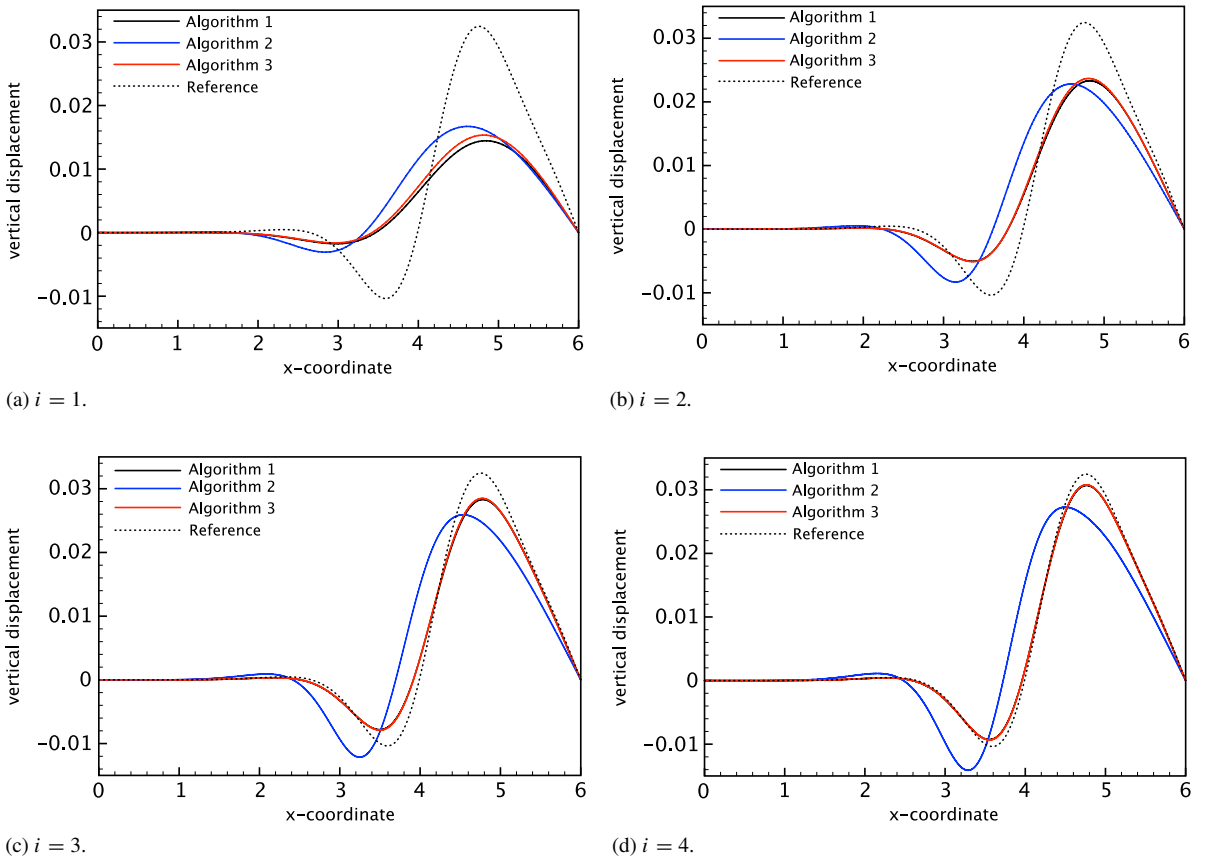

(a) $i = 1$. (b) $i = 2$.

(c) $i = 3$. (d) $i = 4$.

Fig. 4. Implicit vs. explicit coupling. Comparison of the solid displacements at $t = 0.015$ for different levels of (τ, h)-refinement, given by (33) with $i = 1, \ldots, 4$.

The coarsest discretization, $i = 0$, corresponds to the results reported in Figs. 6 and 8. In Fig. 9, we have displayed the interface displacements obtained after successive space–time refinement, $i = 1, \ldots, 4$. These results highlight the convergent behavior of Algorithm 1 and that, after a few space–time refinements, both the fitted and the unfitted methods yield practically the same accuracy.

Fig. 2 reports the convergence history of the solid displacement at time $t = 0.015$, in the relative elastic energy-norm. The results show that Algorithm 1 retrieves the overall optimal $\mathcal{O}(h)$ accuracy of the fitted method. Note that,

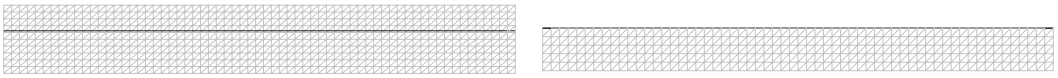

(a) Unfitted: $\Omega^{\mathrm{f}} \subset \Omega^{\mathrm{f}}_{\mathcal{T}_h}$. (b) Fitted: $\Omega^{\mathrm{f}} = \Omega^{\mathrm{f}}_{\mathcal{T}_h}$.

Fig. 5. Computational fluid mesh (in gray) and solid domain (in black).

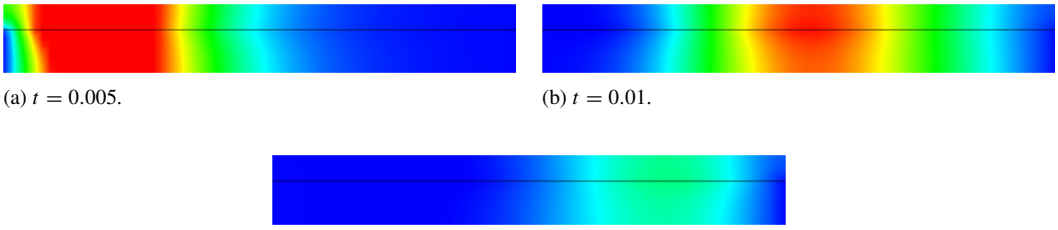

(a) $t = 0.005$. (b) $t = 0.01$.

(c) $t = 0.015$.

Fig. 6. Snapshots of the fluid pressure at different time instants obtained with Algorithm 1.

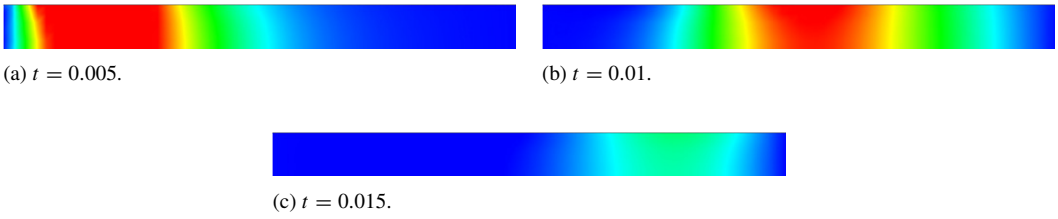

(a) $t = 0.005$. (b) $t = 0.01$.

(c) $t = 0.015$.

Fig. 7. Snapshots of the fluid pressure at different time instants obtained with the fitted method.

owing to Theorem 3.1, the accuracy of Algorithm 1 is expected to be $\mathcal{O}(\tau) + \mathcal{O}(h)$ in the energy norm. Hence, under $\tau = \mathcal{O}(h)$ we retrieve the optimal $\mathcal{O}(h)$ rate observed in Fig. 2.

We discuss now the explicit coupling procedures introduced in Section 4.2. These methods allow an uncoupled time-marching of the fluid and the solid sub-problems. Fig. 3 shows the convergence histories of the solid displacement at time $t = 0.015$, in the relative elastic energy-norm, obtained with Algorithms 1–3 with $K = 1$. The non-convergent behavior of Algorithm 2 under $\tau = \mathcal{O}(h)$ is striking, as anticipated in Section 4.2. On the other hand, Algorithm 3 with one correction step retrieves the overall optimal $\mathcal{O}(h)$ accuracy of the implicit coupling scheme (Algorithm 1). Similar observations can be inferred from Fig. 4, where we have reported the interface displacements obtained with the last four space–time refinements ($i = 1, \ldots, 4$ in (33)).

6. Conclusion

We have introduced a Nitsche type method for incompressible fluid–structure interaction problems with unfitted meshes. The interface is defined as a part of the solid mesh, which is then glued onto the unfitted fluid mesh. The basic ingredients of the method are:

- integration of the fluid equations only in the physical domain (cut elements);
- Nitsche's treatment of the interface coupling conditions (kinematic/kinetic coupling);
- ghost-penalty stabilization to guarantee robustness.

For the space semi-discrete formulation, an a priori error estimate has been derived (Theorem 3.1), which guarantees optimal accuracy with respect to the piecewise affine interpolation used. We have then discussed the stability and accuracy of fully discrete formulations based on implicit and explicit coupling schemes. The numerical results confirmed the theoretical findings. In particular, an overall optimal first-order convergent rate was obtained with the implicit schemes (Algorithm 1) and the explicit coupling scheme with extrapolation/correction (Algorithm 3).

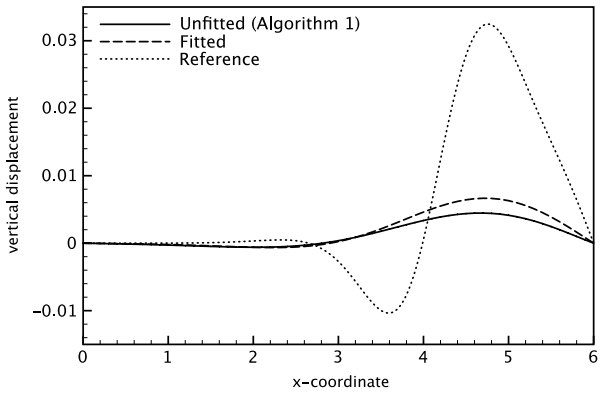

Fig. 8. Comparison of the solid displacements at $t = 0.015$ obtained with $\tau = 2 \cdot 10^{-4}$ and $h = 0.1$.

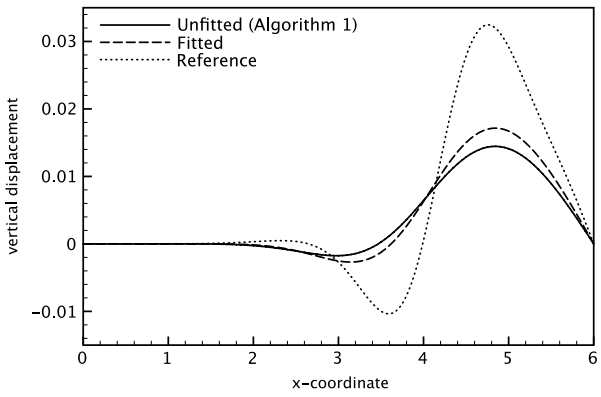

(a) $i = 1$.

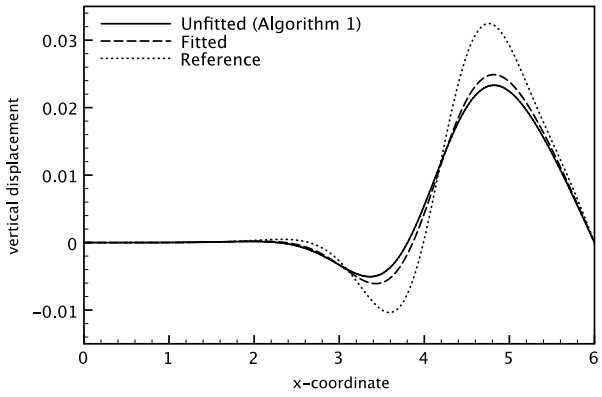

(b) $i = 2$.

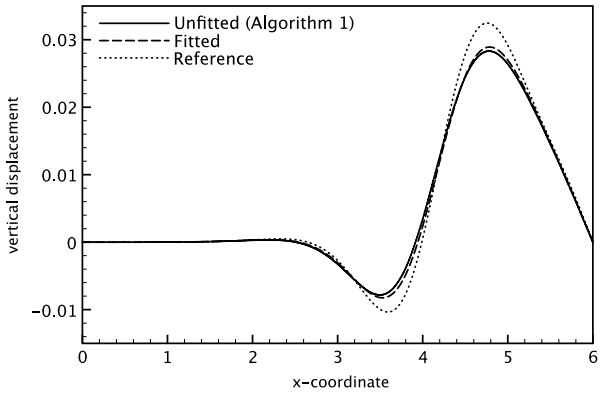

(c) $i = 3$.

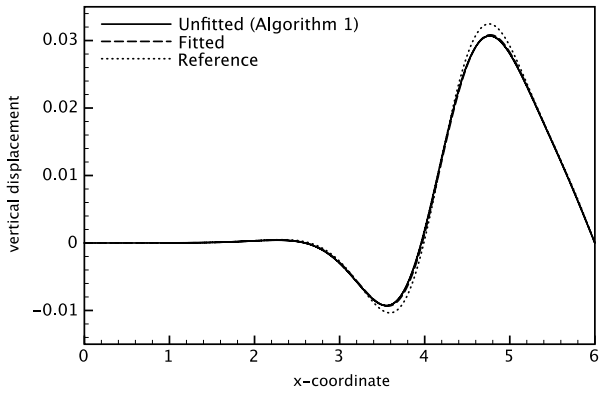

(d) $i = 4$.

Fig. 9. Unfitted vs. fitted methods. Comparison of the solid displacements at $t = 0.015$ for different levels of (τ, h)-refinement, given by (33) with $i = 1, \ldots, 4$.

Further extensions of this work can explore various directions. An important setting, not covered by the present analysis, is the case of moving interfaces. From the computational point of view the case of the coupling with nonlinear fluid and solid models, and the extension to three-dimensional problems also present some interesting challenges. We refer the reader to the recent works [23,28,29] for further discussions of the computational aspects of this type of methods.

Acknowledgments

We would like to thank the reviewers of this paper for their careful reading of the manuscript and their constructive remarks. The first author received funding for this research from EPSRC (award number EP/J002313/1). The second author was supported by the French National Research Agency (ANR) through the EXIFSI project (ANR-12-JS01-0004).

References

[1] P. Hansbo, Nitsche's method for interface problems in computational mechanics, GAMM-Mitt. 28 (2) (2005) 183–206.
[2] A. Hansbo, P. Hansbo, An unfitted finite element method, based on Nitsche's method, for elliptic interface problems, Comput. Methods Appl. Mech. Engrg. 191 (47–48) (2002) 5537–5552.
[3] A. Hansbo, P. Hansbo, A finite element method for the simulation of strong and weak discontinuities in solid mechanics, Comput. Methods Appl. Mech. Engrg. 193 (33–35) (2004) 3523–3540.
[4] E. Burman, P. Hansbo, Fictitious domain finite element methods using cut elements: II. A stabilized Nitsche method, Appl. Numer. Math. 62 (4) (2012) 328–341.
[5] P. Hansbo, J. Hermansson, T. Svedberg, Nitsche's method combined with space–time finite elements for ALE fluid–structure interaction problems, Comput. Methods Appl. Mech. Engrg. 193 (39–41) (2004) 4195–4206.
[6] E. Burman, M. Fernández, Stabilization of explicit coupling in fluid–structure interaction involving fluid incompressibility, Comput. Methods Appl. Mech. Engrg. 198 (5–8) (2009) 766–784.
[7] E. Burman, M.A. Fernández, Explicit strategies for incompressible fluid–structure interaction problems: Nitsche type mortaring versus Robin–Robin coupling, Internat. J. Numer. Methods Engrg. 97 (10) (2014) 739–758.
[8] R. Glowinski, T.-W. Pan, T. Hesla, D. Joseph, A distributed Lagrange multiplier/fictitious domain method for particulate flows, Int. J. Multiphase Flow 25 (5) (1999) 755–794.
[9] C. Peskin, The immersed boundary method, Acta Numer. 11 (2002) 479–517.
[10] F. Baaijens, A fictitious domain/mortar element method for fluid–structure interaction, Internat. J. Numer. Methods Fluids 35 (7) (2001) 743–761.
[11] N. Diniz dos Santos, J.-F. Gerbeau, J.-F. Bourgat, A partitioned fluid–structure algorithm for elastic thin valves with contact, Comput. Methods Appl. Mech. Engrg. 197 (19–20) (2008) 1750–1761.
[12] A. Legay, J. Chessa, T. Belytschko, An Eulerian–Lagrangian method for fluid–structure interaction based on level sets, Comput. Methods Appl. Mech. Engrg. 195 (17–18) (2006) 2070–2087.
[13] A. Gerstenberger, W. Wall, An extended finite element method/Lagrange multiplier based approach for fluid–structure interaction, Comput. Methods Appl. Mech. Engrg. 197 (19–20) (2008) 1699–1714.
[14] D. Boffi, L. Gastaldi, L. Heltai, C.S. Peskin, On the hyper-elastic formulation of the immersed boundary method, Comput. Methods Appl. Mech. Engrg. 197 (25–28) (2008) 2210–2231.
[15] M. Fernández, Coupling schemes for incompressible fluid–structure interaction: implicit, semi-implicit and explicit, SëMA J. (55) (2011) 59–108.
[16] A. Hansbo, P. Hansbo, M.G. Larson, A finite element method on composite grids based on Nitsche's method, M2AN Math. Model. Numer. Anal. 37 (3) (2003) 495–514.
[17] A. Massing, M.G. Larson, A. Logg, M.E. Rognes, A stabilized Nitsche overlapping mesh method for the Stokes problem, Numer. Math. (2014) 1–29. http://dx.doi.org/10.1007/s00211-013-0603-z.
[18] E. Burman, Ghost penalty, C. R. Math. Acad. Sci. Paris 348 (21–22) (2010) 1217–1220.
[19] E. Burman, P. Hansbo, Fictitious domain methods using cut elements: III. A stabilized Nitsche method for Stokes' problem, ESAIM Math. Model. Numer. Anal. 48 (03) (2014) 859–874.
[20] Q. Du, M.D. Gunzburger, L.S. Hou, J. Lee, Analysis of a linear fluid–structure interaction problem, Discrete Contin. Dyn. Syst. 9 (3) (2003) 633–650.
[21] P. Le Tallec, S. Mani, Numerical analysis of a linearised fluid–structure interaction problem, Numer. Math. 87 (2) (2000) 317–354.
[22] F. Brezzi, J. Pitkäranta, On the stabilization of finite element approximations of the Stokes equations, in: Efficient Solutions of Elliptic Systems (Kiel, 1984), in: Notes Numer. Fluid Mech., vol. 10, Friedr. Vieweg, Braunschweig, 1984, pp. 11–19.
[23] A. Massing, M.G. Larson, A. Logg, Efficient implementation of finite element methods on nonmatching and overlapping meshes in three dimensions, SIAM J. Sci. Comput. 35 (1) (2013) C23–C47.
[24] R. Becker, E. Burman, P. Hansbo, A Nitsche extended finite element method for incompressible elasticity with discontinuous modulus of elasticity, Comput. Methods Appl. Mech. Engrg. 198 (41–44) (2009) 3352–3360.
[25] A. Ern, J.-L. Guermond, Theory and Practice of Finite Elements, in: Applied Mathematical Sciences, vol. 159, Springer, 2004.
[26] L. Formaggia, A. Quarteroni, A. Veneziani (Eds.), Cardiovascular Mathematics. Modeling and Simulation of the Circulatory System, in: Modeling, Simulation and Applications, vol. 1, Springer, 2009.
[27] F. Hecht, New development in FreeFem++, J. Numer. Math. 20 (3–4) (2012) 251–265.
[28] B. Schott, W.A. Wall, A new face-oriented stabilized XFEM approach for 2D and 3D incompressible Navier–Stokes equations, Comput. Methods Appl. Mech. Engrg. 276 (2014) 233–265.
[29] E. Burman, S. Claus, H. Hansbo, M. Larson, A. Massing, Cutfem: discretizing geometry and partial differential equations, Internat. J. Numer. Methods Engrg. (2014) submitted for publication.